

Research Paper

The lower dayside ionosphere of Mars from 14 years of MaRS radio science observations



Kerstin Peter^{a,*}, Martin Pätzold^a, Gregorio J. Molina-Cuberos^b, Francisco González-Galindo^c, Olivier Witasse^d, Silvia Tellmann^a, Bernd Häusler^e, Michael K. Bird^{a,f}

^a Abt. Planetenforschung, Rheinisches Institut für Umweltforschung, Cologne, Germany

^b Departamento de Electromagnetismo y Electrónica, Universidad de Murcia, Murcia, Spain

^c Instituto de Astrofísica de Andalucía, CSIC, Granada, Spain

^d Research and Scientific Support Department of ESA, ESTEC, Noordwijk, the Netherlands

^e Universität der Bundeswehr München, Neubiberg, Germany

^f Argelander Institut für Astronomie, Bonn, Germany

ARTICLE INFO

Keywords:

Mars
Radio Science
Mars Express
Ionosphere

ABSTRACT

This work uses a subset of “quiet” MaRS ionospheric dayside observations (MaRS_{quiet}, 2004–2017) and a 1-D photochemical model (IonA-2) to investigate the potential formation processes of the excess electron densities merged with the base of the main ionosphere (Mm). 42% of the investigated MaRS observations contain identified Mm, which occur in a large variety of shapes ranging from smoothly decreasing electron densities to peak structures below the base of M1. The Mm appear over the full range of accessible solar zenith angles (50° - 90°) and are found between approximately 70 and 110 km altitude. Their base is found on average deeper in the atmosphere than the base of the averaged undisturbed MaRS electron density profiles. This indicates a dependence of the Mm formation on energy sources that penetrate deep into the atmosphere. This is supported by a strong positive correlation with increasing solar activity when solar flares, coronal mass ejections, and enhanced short solar X-ray and Ly- α intensities are more common. No relationship is found between the Mm occurrence rate and the magnitude/inclination of the weak crustal magnetic field in MaRS_{quiet}.

Investigations with the IonA-2 photochemical model for undisturbed and flare conditions show that the ionization of the local neutral atmosphere by solar X-ray radiation <2 nm provides a satisfying explanation for detected Mm features with smoothly decreasing electron densities below the M1 base in combination with moderate slopes of the lower Mm region α_{Mm} and altitudes of the lower boundary $h_{L,S}$. While sufficient ionization energy reaches the region of interest during flares, no Mm features with peaks below the M1 base occur in any of the model electron density profiles. This supports the conclusion that the subgroup of merged excess electron densities with peaks or intermediate features (Mi) below the M1 base must have an origin different from the sole variability of solar X-ray radiation during undisturbed and solar flare conditions. The size of the identified Mm makes an exclusive meteoric origin of the Mm peak structures unlikely.

It is indicative from the IonA-2 model results that the general increase/decrease of solar X-ray <2 nm leads to a correlated response of the Mm region. The sporadic occurrence of the merged excess electron densities in the MaRS observations is therefore assumed to be a combination of observational (increased observation noise level compared to the available amount of X-ray radiation <2 nm, shift of the lower baseline by ionospheric deviations from radial symmetry) and environmental (e.g. variations in solar X-ray) factors.

1. Introduction

In situ investigations of planetary ionospheres are constrained by the orbit of the observing spacecraft, and thus there are only limited

opportunities for observing the lower Martian ionosphere. Radio science experiments, however, provide access to the ionospheric electron density by remote sensing. The first radio science observation of the Martian atmosphere and ionosphere was conducted in 1965 by Mariner 4 (Kliore

* Corresponding author.

E-mail address: kerstin.peter@uni-koeln.de (K. Peter).

<https://doi.org/10.1016/j.icarus.2020.114213>

Received 12 September 2019; Received in revised form 21 October 2020; Accepted 11 November 2020

Available online 23 November 2020

0019-1035/© 2020 The Authors.

Published by Elsevier Inc.

This is an open access article under the CC BY-NC-ND license

(<http://creativecommons.org/licenses/by-nc-nd/4.0/>).

et al., 1965). The largest single X-Band radio science data set, consisting of more than 5000 publicly available ionospheric observations, was conducted with the Mars Global Surveyor Spacecraft (MGS – Albee et al., 1998; Hinson et al., 1999; Bougher et al., 2004). These observations, however, were limited to high planetary northern and southern latitudes above 60° . The low circular orbit of 400 km limited the accessible altitude range to below 220–240 km. The Mars Radio Science experiment MaRS (Pätzold et al., 2004) on the Mars Express spacecraft (Fletcher, 2009) began its dual-frequency observations in 2004. More than 900 observations of the neutral atmosphere and ionosphere have been conducted to date. The Mars Atmosphere and Volatile Evolution spacecraft MAVEN (Jakosky et al., 2015a, 2015b) entered orbit around Mars in September 2014, and the MAVEN single X-band Radio Occultation Science Experiment (Withers et al., 2018) began its regular operations in September 2016.

The MaRS electron density profiles in Figs. 1 and 2 illustrate the main and secondary ionospheric peak regions, called M2 and M1, respectively, after nomenclature first used by Rishbeth and Mendillo (2004). While the primary source for the ionization of the M2 region is solar EUV, the dominant sources for the M1 region are solar X-ray and secondary electron impact ionization (Fox et al., 1996). Below the well-established two-layered structure of the dayside ionosphere, Pätzold et al. (2005) discovered small-scale sporadic electron density structures in the observations of the MaRS experiment. Radio science experiments can sense only the ionospheric electron density distribution, but not the

ions. As a result, the origin and ionic composition of these features remained unknown.

The first interpretation of the sporadic excess electron density observations assumed the ablation and ionization of metallic atoms from infalling meteoroids (Pätzold et al., 2005). The possible meteoric origin of this feature has also been investigated in several publications (e.g. Pesnell and Grebowsky, 2000; Molina-Cuberos et al., 2003; Molina-Cuberos et al., 2008; Withers et al., 2008; Whalley and Plane, 2010; Pandya and Haider, 2014; Crismani et al., 2017). However, ions of meteoric origin may not be the only possible source for the excess electron densities. Other potential sources include: (i.) penetration of short solar X-ray and Lyman-alpha ($\text{Ly-}\alpha$) radiation into the planetary upper mesosphere and thermosphere, (ii.) influx of solar energetic particles (SEPs) and (iii.) deviations of the ionospheric electron density from local radial symmetry caused e.g. by internal waves in the neutral atmosphere at mesospheric/thermospheric heights or impact ionization from penetrating solar wind ions (Crismani et al., 2019).

The effect of enhanced solar X-rays on the lower ionosphere is described by models (e.g. Fox, 2004). Mars Global Surveyor radio science observations show an enhancement in the M1 region during solar flares by approximately 200% (Mendillo et al., 2006) and also an enhancement of the M2 region during certain flares (Mahajan et al., 2009). Hydrogen Ly- α radiation (~ 121.6 nm) is the brightest ultraviolet emission feature of the Sun (e.g. Woods et al., 2000; Kockarts, 2002). Its ability to ionize NO molecules makes it a potential candidate for the

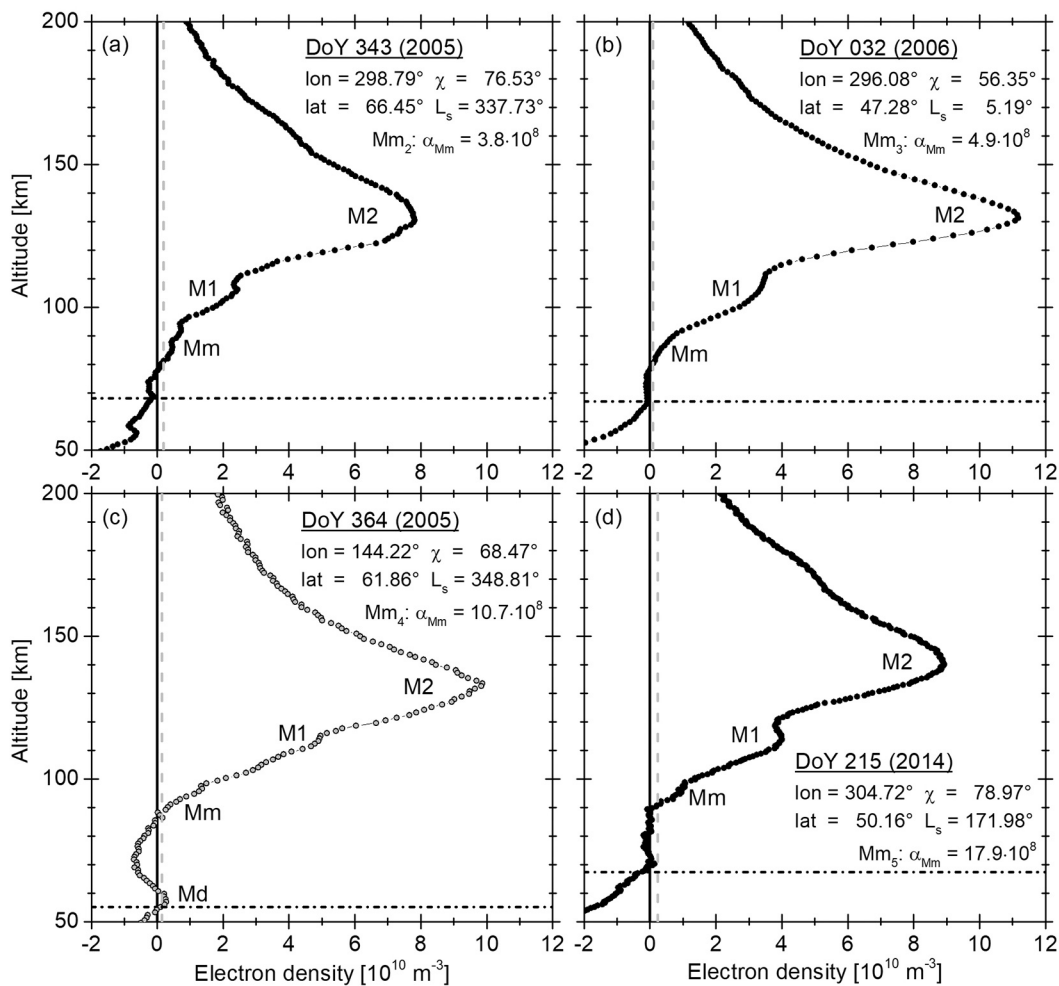


Fig. 1. MaRS radio science observations of the dayside ionosphere of Mars. Black and gray circles show the electron density derived from single X-band n_e^x and differential Doppler n_e^D , respectively. The black straight line is the zero line, the dashed gray line indicates $3\sigma_{nse}$, the black dash-dotted line is the lowest valid altitude $h_{L,val}$. α_{Mm} is the slope of the lower Mm region and further discussed in Section 5 in combination with the Mm_n shape subgroups.

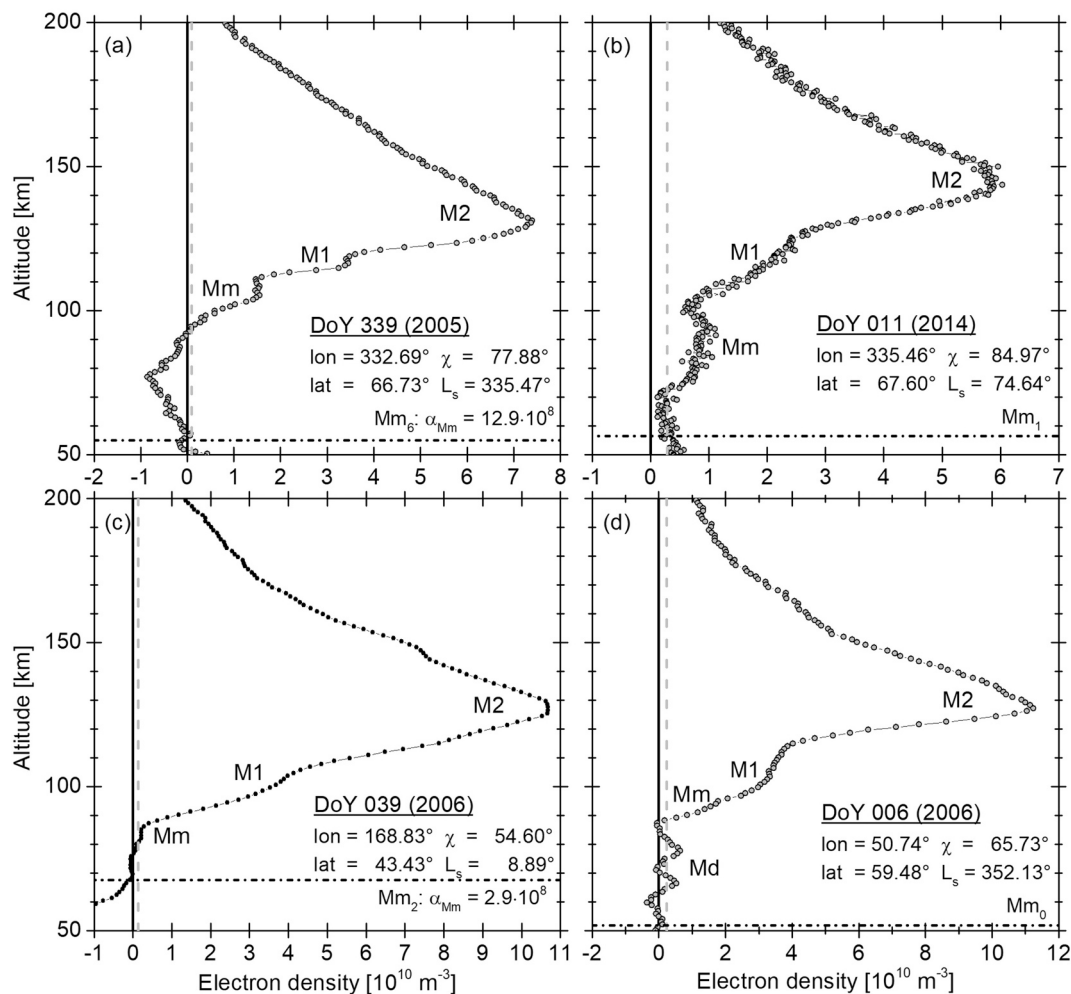


Fig. 2. MaRS radio science observations of the dayside ionosphere of Mars. The labeling of the individual Panels is similar to that of Fig. 1.

formation of excess electron densities in the altitude region of interest below 110 km altitude.

The nitrogen cycle at Mars and therefore the NO/N ratio in the upper mesosphere, however, are not yet well observed (see e.g. Krasnopolsky, 1993; Lefèvre and Krasnopolsky, 2017). The composition of the Mars neutral atmosphere and ionosphere above approximately 110 km altitude was first revealed by the in situ observations of the two Viking landers (Seiff and Kirk, 1977; Soffen, 1977). Whereas neutral NO was identified in the atmosphere, NO⁺ could not be uniquely detected (Hanson et al., 1977). Also no observation of N was made. The neutral gas and ion mass spectrometer NGIMS (Mahaffy et al., 2015a, 2015b) on the MAVEN spacecraft provides regular in situ observations of the Mars neutral atmosphere and ionosphere composition (including N⁺ and NO⁺) down to an approximate spacecraft periapsis altitude of 150 km. Several “deep dips” lowered the MAVEN pericenter altitude to approximately 120 km for a few consecutive orbits. Remote detection of the nitric oxide dayglow (Stevens et al., 2019) by the Imaging UltraViolet Spectrograph IUVS (McClintock et al., 2015) on MAVEN provides first constraints for the NO density in the upper dayside mesosphere of Mars. However, no in situ observations of the atmospheric and ionospheric composition have yet been made in the altitude region of interest between 70 and 110 km altitude.

The currently assumed predominant production mechanism for N and N(²D) in the Mars dayside thermosphere is photodissociation of N₂ by N₂ + hν → N + N(²D). The effect of the photodissociation branching ratio for N₂ on the NO/N ratio in the upper mesosphere is described by Krasnopolsky (1993). Small changes in the production rate of N and

N(²D) are able to change the dominance of either N or NO at 80 km altitude. Electron impact dissociation N₂ + e⁻ → N + N(²D) + e⁻ might provide an additional amount of N and N(²D). De-excitation or quenching of N(²D) during collisions with ambient atoms or molecules changes the ratio between the production of N and N(²D). NO is mainly formed by N(²D) + CO₂ → NO + CO in the thermosphere (Herron, 1999) and potentially by N + CO₂ → NO + CO. The production rate of this latter reaction is approximated by Fox and Sung (2001) as 1.7 · 10⁻²² m⁻³ s⁻¹, based on the investigation of Fernandez et al. (1998). The production of N and NO is balanced by the sink process N + NO → N₂ + O (Burkholder et al., 2015). At night, the recombination of N with O (Du and Dalgarno, 1990) can produce excited NO molecules. The fast and spontaneous de-excitation of NO then produces the Martian ultraviolet nightglow (Bertaux et al., 2005; Stiepen et al., 2017). The nitrogen species (NO or N) with the higher net production is transported downwards from the thermosphere into the upper mesosphere. The primary chemical production mechanisms for NO⁺ in the main ionospheric region include NO + O₂⁺ → NO⁺ + O₂ (Midey and Viggiano, 1999), N + O₂⁺ → NO⁺ + O (Scott et al., 1998), potentially N₂ + O₂⁺ → NO⁺ + NO (upper limit from Fox and Sung, 2001; Ferguson, 1973), and the photoionization of NO. The dominant loss process is dissociative recombination NO⁺ + e⁻ → N(²D) + O (Shuman et al., 2015; Fox, 2015). Photochemical models predict dominance of either NO over N in the upper mesosphere (e.g. Fox, 2004, 2015) or vice versa (e.g. Krasnopolsky, 1993; Lefèvre and Krasnopolsky, 2017, and references therein) due to differences in the particular photochemical reaction scheme.

Solar energetic particles have their origin in the solar corona and are

closely associated with the occurrence of solar flares and coronal mass ejections. Their energy ranges from approximately 1 keV to several GeV and their fluxes can vary by orders of magnitudes within hours/days (e. g. Reames, 1999; Hassler et al., 2012 and references therein). The interruption of surface reflections during MARSIS observations on Mars Express was attributed to SEP impact ionization at altitudes close to or below 100 km (Morgan et al., 2006). Lillis et al. (2010) found, that isolated SEP events coincide with short-lived increases of the total vertical electron content (TEC) by approximately 10^{15} m^{-2} for all solar zenith angles. Uluken et al. (2012) identified a small increase in the ionospheric electron density below 100 km during SEP events, but no clear evidence was found for a general increase in electron density between 100 and 200 km altitude. Potential reservoirs for ionization by solar radiation and SEPs are either local neutral species of planetary origin or metallic neutrals of extraplanetary origin (interplanetary dust particles/remnants of meteoroids).

Internal gravity waves are another potential source for producing excess electron density. Internal waves play an important role in the vertical coupling of the atmosphere/ionosphere system on Earth (see review by Yigit et al., 2016; Yigit and Medvedev, 2015 and references therein). Internal waves are generated by meteorological processes in the lower atmosphere and propagate upward (see e.g. Sánchez-Cano et al. (2018) for Mars). Density disturbances with dominant horizontal scales of 100–300 km, consistent with gravity waves, have been identified in MGS accelerometer data (Creasey et al., 2006). Fritts et al. (2006) determined significant spatial and temporal variability of gravity waves from Mars Global Surveyor and Mars Odyssey aerobraking data. Typical spatial scales are 20–200 km at lower aerobraking altitudes (100–130 km) with density fluctuations from approximately 5 to 50%. A summary of waves detected in the Martian atmosphere, their spatial and temporal characteristics and derived results is available in England et al. (2017), Yigit et al. (2015) and Terada et al. (2017). The occurrence of gravity waves along the ray path during radio sounding observations causes deviations from the radially symmetric ionosphere and neutral atmosphere assumed for the derivation of the atmospheric and ionospheric parameters (a description of the method is available in Fjeldbo and Eshleman, 1965, and Fjeldbo et al., 1971). These deviations can lead to induced variations in the derived MaRS electron density profiles, which would then be interpreted as excess electron densities in the lower ionosphere.

This paper tests the hypothesis that ionization of the ambient neutrals by solar radiation is sufficient to explain the occurrence rate and characteristics of the small-scale sporadic electron density structures observed during “quiet” intervals by MaRS (not disturbed by large solar events). The excess electron densities investigated here are merged with the base of the M1 layer (all Panels of Figs. 1 and 2) and are therefore called merged excess electron densities (Mm). Excess electron densities detached from the lower base of the M1 layer by a region where the electron density values falls below zero are called detached excess electron densities (Md, Panel (c) of Fig. 1 and Panel (d) of Fig. 2), and will be investigated in a future publication. An intermediate structure (called here Mi) between both extremes is shown in Fig. 11 and discussed in Section 6. The paper is structured as follows: Section 2 provides a description of the MaRS ionospheric data set used in this work. Section 3 illustrates the derivation of the observational and environmental parameters. Section 4 describes the derived characteristics of the main features of the lower ionosphere (M2 and M1). Section 5 contains statistical correlations of the Mm occurrences with the derived observational and environmental parameters. Section 6 contains the comparison between the 1-D photochemical IonA-2 model Mm results for changing baseline and solar flare conditions and the observed MaRS Mm characteristics. Finally, Section 7 contains a summary of the derived results and the drawn conclusions. A detailed data analysis for the low noise level MaRS observations between 2004 and 2014 is also found in Peter (2018).

2. The MaRS ionospheric data base

The MaRS radio science experiment sounds the neutral atmosphere and ionosphere by radio signals during Earth occultations (Pätzold et al., 2004, 2009), when the spacecraft moves behind the planetary disk as seen from Earth. During occultation ingress, the continuous radio signal propagates through the atmosphere of Mars from top to bottom and provides information about the state of the ionosphere and neutral atmosphere. MaRS uses simultaneous two-way dual-frequency radio signals at X-Band ($f_{GS,X} \sim 8.4 \text{ GHz}$) and S-Band ($f_{GS,S} \sim 2.1 \text{ GHz}$) (Pätzold et al., 2016). Three ionospheric electron density profiles can be derived: n_e^X from single X-band, n_e^S from single S-band and n_e^D from the frequency residual Δf_{DD} called differential Doppler (DD). The differential frequency residual Δf_{DD} is calculated from the received Doppler shift at the ground station for X-band $\Delta f_{GS,X}$ and S-band $\Delta f_{GS,S}$ by

$$\Delta f_{DD} = \Delta f_{GS,S} - \frac{3}{11} \Delta f_{GS,X} \quad (1)$$

where the factor 3/11 is the ratio of the transmitted S-Band to X-Band frequencies. For ionospheric observations, n_e^X and n_e^D profiles bear the most advantages. The electron density profiles derived from single X-band n_e^X are less sensitive to interplanetary plasma in the path of the radio ray than the electron density profiles derived from single S-band n_e^S . Both, n_e^X and n_e^S are sensitive to unpredicted ground station/spacecraft movements along the line-of-sight. This is not the case for the electron density derived from the differential Doppler n_e^D , which in turn is more sensitive to the ionospheric and interplanetary plasma than n_e^X . The combination of X-Band and S-Band frequencies allows one to distinguish between disturbances introduced by unexpected motion and plasma along the radio ray path (Pätzold et al., 2016).

Fourteen years (2004–2017, Pätzold et al., 2016) of Mars Express MaRS radio science observations provide a large database for the exploration of the characteristics of the ionosphere of Mars. For this paper, MaRS observations with complete dual-frequency recording from the lower base to the upper observational noise level, a solar zenith angle less than 90° , and a low large-scale observational noise $\sigma_{nse,L} < 1 \cdot 10^9 \text{ m}^{-3}$ for either n_e^X or n_e^D have been selected to investigate the lower dayside ionosphere of Mars. $\sigma_{nse,L}$ is a measure for the amount of strong external disturbances during the time of the observation and is calculated with the procedure described in Peter et al. (2014).

The described criteria are met in 289 profiles for the MaRS_{quiet} data set, each one consisting of either the n_e^X or the n_e^D profile for each MaRS occultation, depending on the lower $\sigma_{nse,L}$ value.

3. Derived observational and environmental parameters

For each MaRS observation the derived observational parameters comprise the solar longitude L_S , the planetocentric longitude lon and latitude lat, the solar zenith angle χ and the areoid altitude defined at that time when the spacecraft was sounding the ionosphere at 130 km altitude above the areoid. The parameter set does also contain the general upper baseline noise level σ_{nse} , the lowest valid altitude $h_{L,val}$, the characteristics of the M2/M1 ionospheric regions and the occurrence rate and characteristics of the merged excess electron densities.

The upper baseline noise level σ_{nse} of an electron density profile is the standard deviation of the electron density samples above the local areoid altitude +800 km. The offset of the upper baseline μ_{UB} is the mean electron density calculated for the same altitude range. It is expected that an undisturbed ionospheric electron density profile in a radial-symmetric ionosphere would provide $\mu_{UB} = 0$ in a region with neutral and ionospheric densities below the detection limit. However, there are always residual disturbances in the electron density. Therefore all MaRS electron density profiles are calibrated by subtracting μ_{UB} . This procedure avoids a bias in the extracted observational parameters, e.g. a potential increase in total vertical electron content caused by a shift of

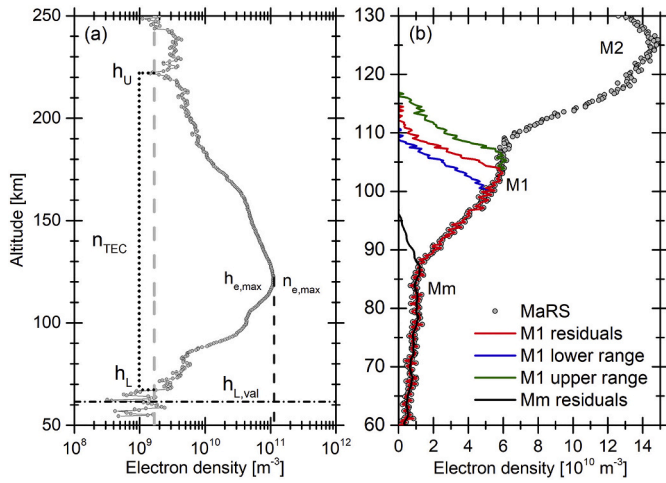


Fig. 3. (a) Selected observational parameters for the n_e^D MaRS observation of DoY 111 (2006), $L_S = 42.32^\circ$, $\text{lon} = 158.17^\circ$, $\text{lat} = 7.38^\circ$, $\chi = 58.80^\circ$. (b) Derived M1 and Mm characteristics for the MaRS observation of DoY 337 (2013), $L_S = 57.59^\circ$, $\text{lon} = 56.99^\circ$, $\text{lat} = 17.69^\circ$, $\chi = 57.16^\circ$. Gray circles show the original MaRS data. Red, blue and green lines indicate the electron density residuals for the M1 parameter determination with lower and upper ranges. The residuals are determined from associated line fits (not shown). The black line indicates the Mm residuals. A further description of the M1 parameter determination is found in [Appendix B](#). (For interpretation of the references to colour in this figure legend, the reader is referred to the web version of this article.)

the whole profile to higher electron densities. The lowest valid altitude $h_{L,\text{val}}$ is defined as that altitude where the neutral atmosphere is strong enough to bias the observation of the ionospheric electron density. It is chosen to be that altitude below the ionospheric main peak at which the negative electron density exceeds $-3\sigma_{nse}$ in n_e^X for the last time (see [Appendix A](#) for details).

The vertical electron content (TEC) n_{TEC} is derived by integrating the electron density between the upper border h_U and the lower border h_L of the ionospheric profile

$$n_{TEC} = \int_{h_L}^{h_U} n_e(h) dh \quad (2)$$

h_U and h_L are those altitudes, where the electron density appears from and disappears into the background noise $3\sigma_{nse}$.

In addition to h_L and h_U , $h_{L,S}$ and $h_{U,S}$ are retrieved from the smoothed electron density $n_{e,S}$ derived with the smoothing algorithm described below. $h_{L,S}$ and $h_{U,S}$ are later used to determine the extent of the Mm region. Those parameters, the M2 peak electron density $n_{e,\text{max}}(M2)$ and M2 peak altitude $h_{\text{max}}(M2)$ are illustrated in [Fig. 3a](#). $n_{e,\text{max}}(M2)$ and $h_{\text{max}}(M2)$ are determined from the MaRS electron density profiles without any further data manipulation. The associated error bars are calculated with the procedures described in [Peter et al., 2014](#).

The M1 region in the electron density profiles appears either as a pronounced layer ([Fig. 1d](#)) or as a shoulder shape below the base of M2 (e.g. [Fig. 1b](#)). The M1 TEC $n_{TEC}(M1)$, peak electron density $n_{e,\text{max}}(M1)$ and peak altitude $h_{\text{max}}(M1)$ cannot be derived directly from the observations in the latter case. An automated procedure is applied to the

MaRS_{quiet} data set to derive the M1 and Mm characteristics for all observations (details in [Appendix B](#)). The most reliable Mm parameters are the lower altitude extent $h_{L,S}$ and the vertical TEC $n_{TEC}(Mm)$. $h_{L,S}$ is the only parameter not biased by the presence of M1 and $n_{TEC}(Mm)$ is an estimate for the visible vertical TEC of the merged excess electron density region. Only those features with $n_{TEC}(Mm) > 3,000 \cdot 3\sigma_{nse}$ are identified as Mm to avoid a bias of the statistics by small scale electron density fluctuations.

Given the importance of the EUV and X-ray solar flux and of the crustal magnetic field in determining the ionospheric behavior (e.g. [Withers, 2009](#)), it is important to derive proxies for them for each observation in the MaRS_{quiet} data set. Before the arrival of MAVEN in September 2014, no direct solar flux observations at the position of Mars were available. Therefore solar flux proxies for the complete MaRS_{quiet} data set were derived from the Solar Irradiance Platform (SIP) V2.38 ([Tobiska et al., 2000](#)) solar flux for Earth. The SIP V2.38 model provides one averaged solar spectrum per day at different spectral resolutions. The SIP V2.38 1 nm resolution VUV2002 FUV-UV spectra are temporally and spatially calibrated to the Mars position by using the method described in [Peter et al. \(2014\)](#). The derived solar flux proxy $\phi_{\leq 95}^M$ contains the integrated solar flux from 0.45 to 95 nm at the Mars position ([Table 1](#)). It is an approximation for the ionizing solar flux at the top of the Martian atmosphere at the time of a MaRS observation. The minimum wavelength of 0.45 nm is chosen because the SIP 0.1 nm resolution spectra do not contain entries below 0.5 nm. $\phi_{\leq 10}^M$ contains the integrated solar flux from 0.45 to 10 nm, while $\phi_{\leq 3}^M$ contains the integrated solar flux from 0.45 to 3 nm at the Mars position. $\phi_{\leq 10}^M$ is the solar flux capable of ionizing the M1 region. $\phi_{\leq 3}^M$ indicates a flux range capable of reaching the base of the ionosphere. $\phi_{\leq 95}^E$ contains the SIP V2.38 solar flux from 0.45 to 95 nm at Earth position without any further calibration. $\phi_{\leq 95}^E$ is a proxy for the activity of the Sun, which is not immediately apparent from $\phi_{\leq 95}^M$ because of the large solar flux variation at the top of the Martian atmosphere caused by the eccentricity of the Mars orbit (see [Fig. 4](#)). The $\phi_{121.5}^M$ solar proxy provides an estimate for the Ly- α radiation available at Mars. Low, moderate and high solar flux proxy ranges ([Table 1](#)) are determined from the available fluxes in the MaRS_{quiet} data set and therefore describe relative, but not absolute flux boundaries for different solar activity levels. The lower and upper flux proxy boundaries for $\phi_{\leq 95}^M$, $\phi_{\leq 10}^M$, $\phi_{\leq 3}^E$ and $\phi_{121.5}^M$ are defined by the 1- σ standard deviation of the mean flux μ . Because of the high variability of the short solar X-ray flux, the boundaries for $\phi_{\leq 3}^M$ are set by $\mu \pm 0.5\sigma$.

The average magnitude of the crustal magnetic field B_{tot} and field inclination angle Θ_{incl} for each MaRS observation are derived from the spherical harmonic model of the lithospheric magnetic field of Mars developed by [Morschhauser et al. \(2014\)](#). The model expresses the magnetic field in terms of the components pointing horizontally north (B_x), east (B_y), and vertically down (B_z). The magnitude of the magnetic field is determined by $(B_x^2 + B_y^2 + B_z^2)^{1/2}$. The derived field inclination is the angle between $-B_z$ and $(B_x^2 + B_y^2)^{1/2}$. A positive inclination angle therefore indicates an upward curvature, while a negative inclination angle indicates a downward curvature of the magnetic field lines. B_{tot} and Θ_{incl} are calculated by averaging the derived magnitude of the crustal magnetic field and the field inclination angle for the coordinates of each MaRS observation point within the region of interest between 70 and 120 km altitude.

Table 1
Derived solar flux proxies and their boundaries.

Flux proxies	Integr. Range	Calibration	Units	Low	Moderate	High
$\phi_{\leq 95}^M$	0.45–95 nm	Mars	$[10^{14} \text{ s}^{-1} \text{ m}^{-2}]$	$\Phi < 1.85$	$1.85 \leq \Phi \leq 2.48$	$\Phi > 2.48$
$\phi_{\leq 10}^M$	0.45–10 nm	Mars	$[10^{12} \text{ s}^{-1} \text{ m}^{-2}]$	$\Phi < 2.13$	$2.13 \leq \Phi \leq 3.26$	$\Phi > 3.26$
$\phi_{\leq 3}^M$	0.45–3 nm	Mars	$[10^{11} \text{ s}^{-1} \text{ m}^{-2}]$	$\Phi < 3.17$	$3.17 \leq \Phi \leq 4.91$	$\Phi > 4.91$
$\phi_{\leq 95}^E$	0.45–95 nm	Earth/none	$[10^{14} \text{ s}^{-1} \text{ m}^{-2}]$	$\Phi < 4.61$	$4.61 \leq \Phi \leq 5.60$	$\Phi > 5.60$
$\phi_{121.5}^M$	121–122 nm	Mars	$[10^{15} \text{ s}^{-1} \text{ m}^{-2}]$	$\Phi < 1.41$	$1.41 \leq \Phi \leq 1.85$	$\Phi > 1.85$

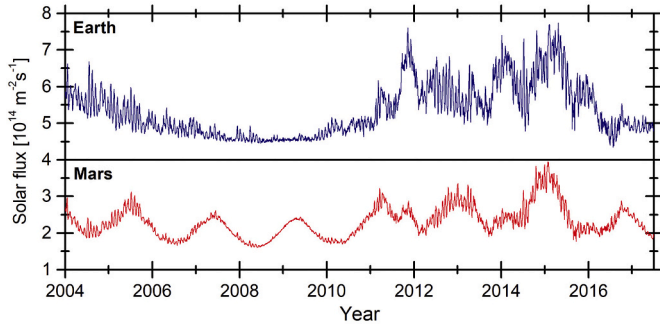


Fig. 4. Upper Panel: Integrated SIP V2.38 solar flux between 0.45 and 95 nm without further calibration ($\phi_{\leq 95}^E$). Lower Panel: Integrated SIP V2.38 solar flux between 0.45 and 95 nm calibrated for the Mars position ($\phi_{\leq 95}^M$).

4. Characteristics of the main ionospheric features

Fig. 5 summarizes the derived M2 and M1 features in dependence of the solar zenith angle and the solar flux proxies associated with each individual MaRS observation. The vertical TEC of the whole ionospheric profile n_{TEC} , peak electron density $n_{e,max}(M2)$ and peak altitude $h_{max}(M2)$ are shown in dependence of $\Phi_{\leq 95}^M$. The characteristics of the

M1 feature are shown in dependence of $\Phi_{\leq 10}^M$, except for the M1 altitude which is shown in dependence of $\Phi_{\leq 95}^M$. Only the derived error bars for the $\phi_{\leq 95}^M$ and $\phi_{\leq 10}^M$ groups are shown for clarity. The green squares are the weighted means in each panel. The weighted mean \bar{X}_w is computed from

$$\bar{X}_w = \frac{\sum_{i=1}^N \frac{1}{\sigma_{X,i}} \cdot X_i}{\sum_{i=1}^N \frac{1}{\sigma_{X,i}}}, \quad (3)$$

where N is the number of the data points X_i with the error $\sigma_{X,i}$ in each 5° solar zenith angle interval.

Fig. 5a illustrates the relation between n_{TEC} and $\Phi_{\leq 95}^M$. Most MaRS_{quiet} observations in the $\Phi_{\leq 95,low}^M$ interval are found below the weighted average \bar{n}_{TEC} , while the MaRS_{quiet} observations for $\Phi_{\leq 95,high}^M$ are mostly found above. Peter et al. (2014) used a smaller data set and found a similar correlation between n_{TEC} and absolute solar activity proxies. The M1 vertical TEC $n_{TEC}(M1)$ in Panel (b) of Fig. 5 shows a similar correlation with $\Phi_{\leq 10}^M$. This relation is also valid for the magnitude of the M2 and M1 peak electron densities (Panel c, d). This expected correlation between input radiation and ionospheric magnitude shows, that the chosen solar flux proxies are valid even if they were derived from a model developed for Earth. Panel (e) shows the correlation between $h_{max}(M2)$ and $\Phi_{\leq 95}^M$, while Panel (f) shows the correlation between

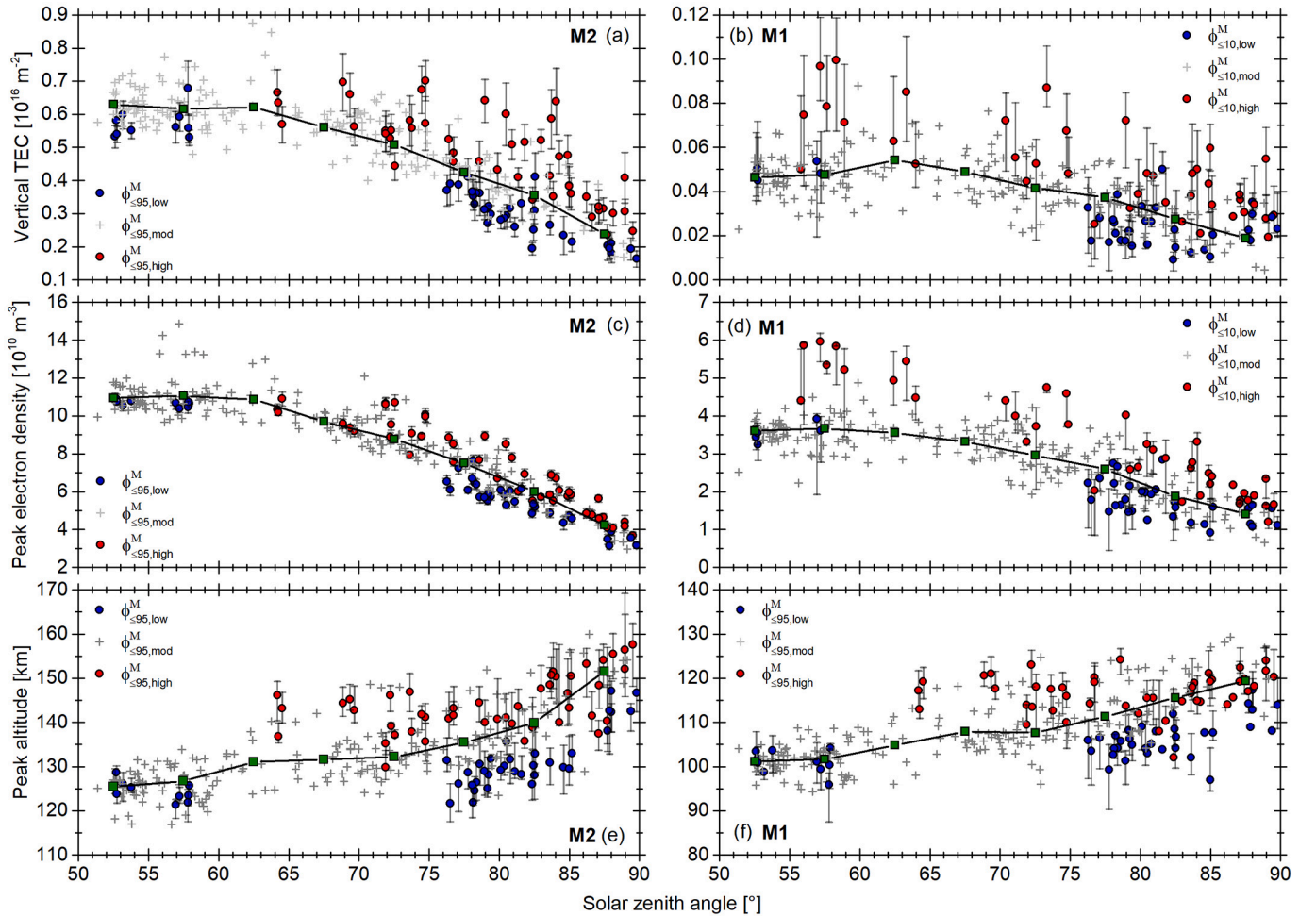


Fig. 5. Characteristics of the main ionospheric features. Panel (a), (c) and (e) show the features of the M2 region, while Panel (b), (d) and (f) show the features of the M1 region. The green squares are the weighted average of the $\phi_{\leq 95,mod}^M$ data in 5° solar zenith angle bins. (For interpretation of the references to colour in this figure legend, the reader is referred to the web version of this article.)

$h_{max}(M1)$ and $\Phi_{\leq 95}^M$. $\Phi_{\leq 95}^M$ is chosen for a potential correlation with $h_{max}(M1)$, because the altitude of the main ionospheric body is closely related to that altitude, where most ionizing solar radiation is absorbed. This altitude depends on the density distribution of the neutral atmosphere, which in turn depends on the neutral temperature distribution. The neutral temperature distribution is affected by solar heating of the atmosphere, which is better represented by $\Phi_{\leq 95}^M$ than by $\Phi_{\leq 10}^M$. The effect of floating dust on the ionospheric peak (e.g. Wang and Nielsen, 2003) will be investigated in a future publication.

5. Statistical correlations of the merged excess densities with observational and environmental parameters

5.1. Mm characteristics in dependence of solar zenith angle and solar flux

The full MaRS_{quiet} data set contains approximately 42% merged excess electron density features Mm. Their distribution is shown in Fig. 6, where the identified Mm cover the full solar zenith angle range accessible with the MaRS_{quiet} data from 50° to 90°. No clear correlation is found between the occurrence rate of the merged excess electron densities P_{Mm} and χ .

Table 2 illustrates the potential correlations between the Mm occurrence rate P_{Mm} and the derived solar proxies $\phi_{\leq 95}^M$, $\phi_{\leq 10}^M$, $\phi_{\leq 3}^M$, $\phi_{\leq 95}^E$ and $\phi_{121.5}^M$. P_{Mm} is strongly correlated with the Sun's activity, indicated by the increase of P_{Mm} for increasing $\phi_{\leq 95}^E$. This highlights the importance of the Sun's solar activity level in the formation process of the merged excess electron densities. Solar events, which provide potential energy sources for the Mm in the form of background short X-ray flux are rare for low solar activity (Aschwanden, 1994), as are CMEs (Gopalswamy, 2016) and strong solar flares (Hathaway, 2015). Also the solar Ly- α radiation increases for increasing solar activity (Woods et al., 2000), which is a potential source for NO ionization. No correlation is found between P_{Mm} and the other individually derived flux proxies. $\phi_{\leq 95}^M$ and $\phi_{\leq 10}^M$ represent the general ionizing flux for the ionosphere and might contain a spectrum too wide for a direct correlation with P_{Mm} . $\phi_{\leq 3}^M$ is a proxy for the short solar X-ray radiation at Mars. The SIP V2.38 output of only one solar spectrum per Earth day might, however, not be sufficient to capture the highly variable solar X-ray output of the Sun at the Mars position. No direct correlation is found between P_{Mm} and $\phi_{121.5}^M$, which indicates no strong effect of the Ly- α variability on the Mm formation in the MaRS_{quiet} data set.

Fig. 7(a) compares the altitude $h_{L,S}$ of the ionospheric base of the

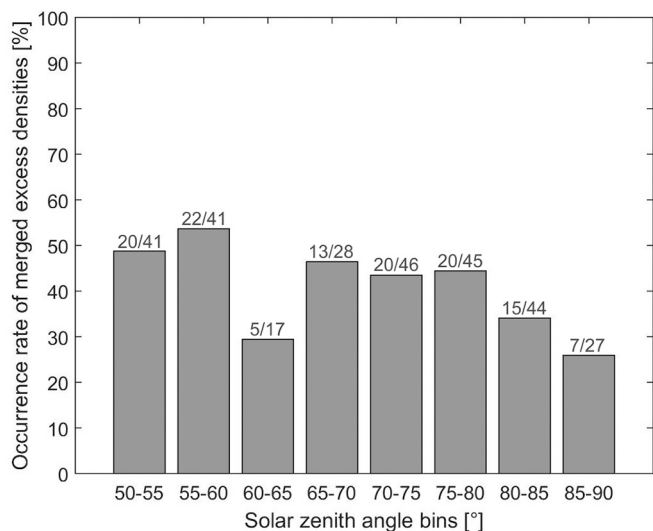


Fig. 6. Mm occurrence rates in 5° solar zenith angle bins. The number combination x/y above the columns is: x = number of identified merged excess electron densities and y = all MaRS observations in that solar zenith angle bin.

MaRS observation with and without identified merged excess electron densities. The smoothed ionospheric base of the merged excess electron densities is on average lower in the Martian atmosphere than the base of the smoothed undisturbed observations. This fact is even better visible in Panel (b) of Fig. 7, where the mean and standard deviation of $h_{L,S}$ are plotted for the disturbed and the undisturbed observations. This indicates a formation process for the merged excess electron densities where certain energy sources penetrate the Mars ionosphere deeper than ionization sources for the undisturbed ionosphere. Potential candidates are photons with extremely short wavelengths or solar energetic particles. The ionization of NO by Ly- α radiation is another possibility, but no direct correlation between $\phi_{121.5}^M$ and P_{Mm} has been identified.

n_{TEC} , $n_{e,max}(M2)$, $n_{TEC}(M1)$ and $n_{e,max}(M1)$ show a direct correlation with both the solar zenith angle and either $\phi_{\leq 95}^M$ or $\phi_{\leq 10}^M$, respectively (Fig. 5). However, neither the vertical TEC nor the maximum electron density of the Mm (Fig. 8) show a correlation with χ or $\phi_{\leq 3}^M$. As stated earlier, a likely reason for the missing correlation with $\phi_{\leq 3}^M$ is that the Sun's variability in the short solar X-ray at the Mars position during the time of a MaRS observation might not be sufficiently represented by the proxy. A potential solar zenith angle dependence of $n_{TEC}(Mm)$ and $n_{e,max}(Mm)$ might also be obscured by the high variability of solar X-ray radiation < 3 nm.

The detected Mm comprise a large variety of shapes (Table 3). The division into different types is conducted on a phenomenological base due to the unclear origin of the individual Mm features. The shape determination is feasible for MaRS observations only where the Mm altitude range extends 3 km or more below maximum. Mm with peak structures below the base of M1 (category Mm₁) are determined with a method related to that described in Withers et al. (2008). $n_{e,S}$ is searched for peaks between $h_{U,S}$ and $h_{L,S}$. A peak structure (Fig. 2b) is identified if $n_e(h_i) - n_e(h_j) > 3\sigma_{nse}$ for $h_i - h_j = 5$ km and $i > j$. A straight line fit on $n_{e,S}$ between $h_{L,S}$ and $h_{max}(Mm) - 0.5$ km yields the base for the definition of the remaining Mm types. The derived slope of the lower Mm region α_{Mm} and the maximum difference δ_{Mm} between the fitted line and $n_{e,S}$ in the region of interest provide the parameters for the Mm shape groups Mm₂ – Mm₆ (examples in Figs. 1 and 2). 2.5% of the MaRS_{quiet} observations contain peaks below M1, which is slightly larger than the 1% found by Withers et al. (2008). The authors, however, did not include detections with a peak density < $1.0 \cdot 10^{10} \text{ m}^{-3}$. This additional constraint results in only 2 remaining electron density profiles with pronounced peaks in MaRS_{quiet} (0.7%). MaRS observations with larger external disturbances (not investigated here) might, however, increase the number of peak detections in MaRS observations. Due to the fact that also all Md contain peak structures by definition, an investigation of the Md will also increase the identified number of peaks in the lower ionosphere.

5.2. Mm characteristics in dependence of the presence of crustal magnetic fields

Wind shear (Whitehead, 1960; Mathews, 1998) is a widely accepted theory for the origin of certain sporadic E layers in the lower Earth ionosphere. The zonal/meridional wind shear mechanisms (e.g. Shinagawa et al., 2017) describe the convergence of long living metallic ions into small spatial but high density ionospheric layers in wind shear regions under the influence of the varying orientations the global magnetic field. Potential mechanisms for the formation of sporadic layers of metal ions with meteoroidic origin on Mars are discussed in Grebowsky et al. (2017). Wind shear as a potential formation mechanism for the merged excess electron densities on Mars essentially requires the presence of a magnetic field. No information about the wind direction and velocity in ionospheric altitudes is available from the MaRS observations. It can therefore only be tested if any correlation between the Mm occurrence rate P_{Mm} and the average magnitude (B_{10}) and inclination (Θ_{incl}) of the crustal magnetic field between 70 and 120 km altitude of the MaRS observation exists. The distribution of the MaRS_{quiet} observations in Table 4 shows that the bulk of the observations was conducted

Table 2
Occurrence rate of the merged excess electron densities in dependence of the derived solar flux proxies.

Flux level	Proxy	All	Mm	[%]	Proxy	All	Mm	[%]	Proxy	All	Mm	[%]
Low	$\phi_{\leq 95}^M$	43	16	37.2	$\phi_{\leq 3}^M$	102	43	42.2	$\phi_{\leq 95}^E$	26	7	26.9
Mod.		200	91	45.5		145	60	41.4		225	96	42.7
High		46	15	32.6		42	19	45.2		38	19	50.0
Low	$\phi_{\leq 10}^M$	38	13	34.2	$\phi_{121.5}^M$	41	16	39.0				
Mod.		210	92	43.8		193	92	47.7				
High		41	17	41.5		41	14	25.4				

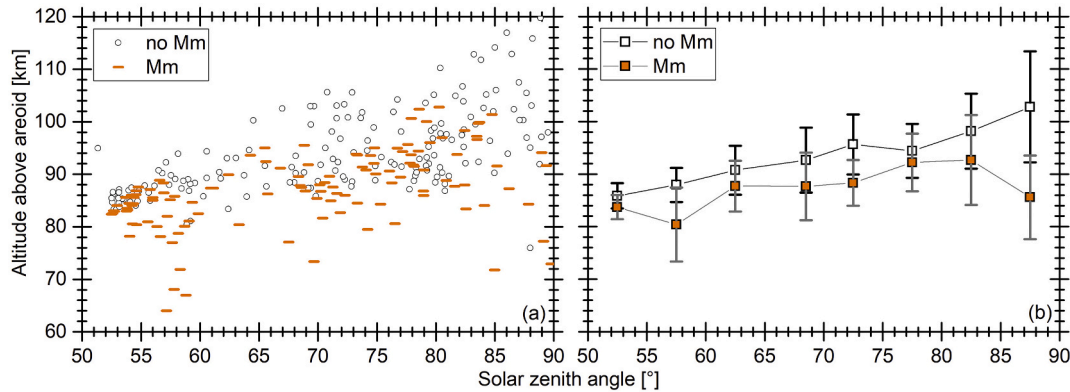


Fig. 7. (a) Lower ionospheric boundary $h_{L,S}$ for the MaRSquiet observations with and without identified Mm. (b) Mean and standard deviation of $h_{L,S}$ in 5° solar zenith angle bins, separately calculated for the observations with and without Mm.

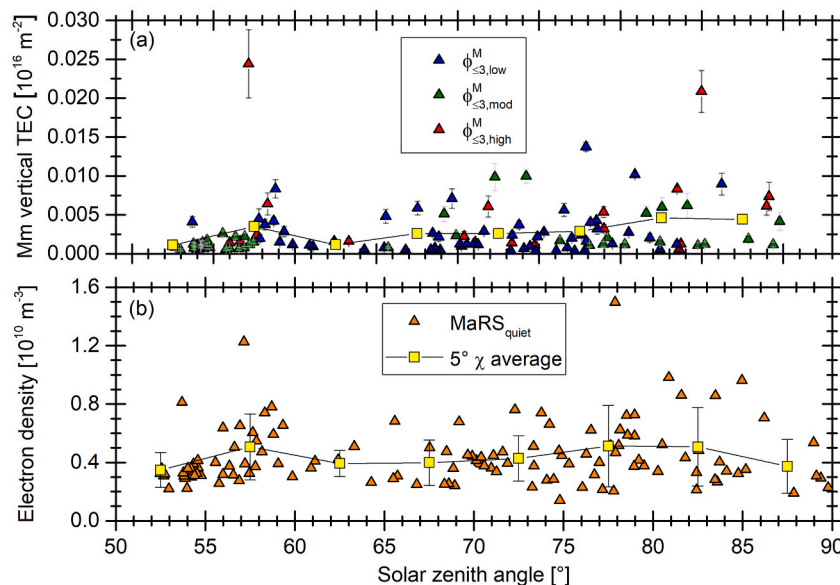


Fig. 8. (a) Mm vertical TEC in dependence of the $\phi_{\leq 3}^M$ proxy intervals with 5° solar zenith angle bin mean. The large TEC range causes a standard deviation including negative TEC values. Therefore the standard deviation is not shown. (b) Mm electron density with 5° solar zenith angle bin mean and standard deviation.

over weak crustal magnetic field regions. The 71 observation summarized in the last table row contain observations ranging from 50 to a maximum of ~ 1800 nT. Due to the sparse observational coverage of the high magnetic field range, the selected data set is inconclusive concerning the correlation between P_{Mm} and very large B_{tot} . No clear correlation is found between the increasing magnitude of the magnetic field and the Mm occurrence rate. This is also true for the Mm distribution and the reduced Mm distribution in comparison with the field line inclination angles (Fig. 9). Under the assumption, that neutral winds did not drag away most Mm from their point of origin, the high number of observed Mm over weak crustal fields indicates that wind shear is an

unlikely source for the majority of the identified merged excess electron densities in MaRSquiet.

6. Comparing the model merged excess electron densities with the Mm observed by MaRS

Radio occultations provide observations of the ionospheric electron density distribution, but no information about the corresponding ions. The potential Mm formation by solar X-ray and the effect of a changing neutral atmosphere on the Mm composition are therefore studied with a 1-D ionospheric model. The NO/N ratio in the upper mesosphere is not

Table 3

Mm shape distribution. The „Reduced“ column provides the Mm percentage distribution within the Mm₁ to Mm₆ subgroups. α_{Mm} is provided in $10^{-5} m^{-4}$.

Category	MaRS occultations		
	Mm [#]	All [%]	Reduced [%]
Mm ₀ : Mm extent below peak <3 km	66	54.1	–
Mm ₁ : Peaks	7	5.7	12.5
Mm ₂ : $\delta_{Mm} < \sigma_{nse}$ $\alpha_{Mm} < 4.0$	15	12.3	26.8
Mm ₃ : $\delta_{Mm} < \sigma_{nse}$ $4.0 \leq \alpha_{Mm} < 8.0$	13	10.7	23.2
Mm ₄ : $\delta_{Mm} < \sigma_{nse}$ $8.0 \leq \alpha_{Mm} < 12.0$	4	3.3	7.1
Mm ₅ : $\delta_{Mm} < \sigma_{nse}$ $\alpha_{Mm} > 12.0$	4	3.3	7.1
Mm ₆ : $\delta_{Mm} \geq \sigma_{nse}$ –	13	10.7	23.2

Table 4

B_{tot} distribution in the MaRS_{quiet} data set.

B_{tot} range [nT]	MaRS occultations		
	All [#]	Mm [#]	Mm [%]
0–10	106	46	43.4
10–20	51	25	49.0
20–30	28	13	46.4
30–40	19	6	31.6
40–50	14	8	57.1
>50	71	24	33.8

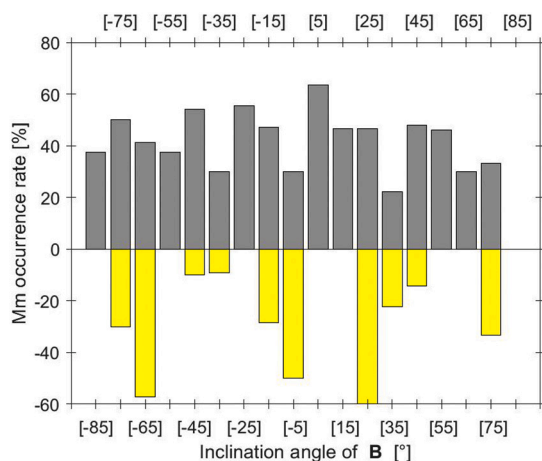


Fig. 9. Mm occurrence rate in 10° bins of Θ_{incl} . Positive P_{Mm} indicate the distribution based on the whole MaRS_{quiet} data set, negative P_{Mm} indicate the reduced distribution based on all MaRS_{quiet} observation where $B_{tot} > 10$ nT.

yet well determined from observations, therefore three model scenarios with different nitrogen chemistry are applied.

IonA-2 (Ionization in Atmospheres - 2) is a time-marching photochemical transport model with an implemented diurnal cycle. The simulation of the diurnal cycle in IonA-2 uses the Mars Climate Database (MCD) V5.2 (Lewis et al., 1999; Millour et al., 2015) primary neutral species and neutral temperature for a full Martian Sol derived at the planetary longitude and latitude of the modeled MaRS observation. Two kinds of solar flux spectra are applied: static and dynamic. The static spectra are either derived from the SIP V2.38 model (1 solar flux spectrum/24 h, calibration described in Peter et al. (2014)) or a combination of SIP V2.38 (> 10 nm) and the FISM flare V2.0 model (Chamberlin et al. (2007), 1 solar spectrum/60s, 0.1 nm spectral resolution) for solar radiation ≤ 10 nm. The response of the Martian ionosphere to solar flares is investigated by applying a series of FISM flare spectra. The derivation and calibration of the FISM spectra is found in Appendix D. The MCD primary neutral species (Table 5), neutral temperature and photoionization calculated from solar radiation are updated every model time step based on the current planetary local time and solar zenith angle. The

Table 5

IonA-2 model parameters.

Model description	1-D time marching photochemical model with diurnal cycle 65–300 km altitude, 1 km altitude resolution
Planetary parameters	Planetary coordinates derived from the selected MaRS observation
Primary species	CO ₂ , N ₂ , O ₃ , O, H ₂ O, O ₂ , H, Ar, CO, H ₂
Temperature	$T_N = T_{15}$, T_e from Rohrbaugh et al. (1979)
Solar flux	Static spectra: SIP V2.38 VUV2002 FUV-UV spectrum, calibrated for the position of Mars SIP V2.38 VUV2002 FUV-UV (> 10 nm) + FISM V2.0 flare (≤ 10 nm) 0.1 nm spectral resolution, calibrated for the distance of Mars Dynamic spectra: SIP V2.38 VUV2002 FUV-UV (> 10 nm) + FISM V2.0 flare (≤ 10 nm), 60s temporal resolution, 0.1 nm spectral resolution, calibrated for the distance of Mars
Photo-absorption/dissociation and ionization cross sections	Huebner and Mukherjee (2015) for all species except O ₃ (Sander et al., 2011), CO ₂ and N ₂ (see summary in Peter, 2018)
Secondary ionization	W-value approach (Wedlund et al., 2011)
Transport	Eddy diffusion, minor molecular diffusion and ambipolar diffusion
Time step	60 s
Convergence	maximum change of the N, N(² D) and NO densities at each altitude falls below 3.5% at a predefined local time from one Sol to the next IonA-2 _{flux} /IonA-2 _{flux,N} : Limiting velocities at the homopause $w_s = K/H_N$ (Hunten, 1973) with the eddy diffusion coefficient K and the neutral scale height H_N for N and NO in combination with the locally available densities at each time step of the computation; zero for all other species. IonA-2 _{part} : Limiting velocities at the homopause w_s reduced by factor 100.
Lower boundary flux conditions for molecular diffusion	

photochemical scheme in combination with eddy and minor neutral molecular diffusion and ambipolar diffusion of the ions provides vertical profiles of several secondary neutral species (C, H₂O₂, HO₂, O(¹D), N(²D), N, NO, NO₂ and OH) and ions (Ar⁺, CO₂⁺, CO⁺, C⁺, HCO₂⁺, HCO⁺, H⁺, N₂⁺, NO⁺, N⁺, O₂⁺ and O⁺) for a full Martian Sol (see Appendix C and Peter (2018) for further IonA-2 model details).

Fig. 10 shows the neutral atmosphere and ionosphere profiles as modeled by IonA-2 for the observation parameters of DoY 336 (2005) and the SIP V2.38 solar radiation. This MaRS observation contains a Mm₃ Mm structure ($\alpha_{Mm} = 4.1 \cdot 10^{-5} m^{-4}$). After decreasing below $3\sigma_{nse}$, but not below zero, n_e shows an additional small structure in the lower Mm region (see also Fig. 11) not fully disconnected from the main ionospheric body (Mi, intermediate). The behavior of the Mm structure is discussed in Sections 6.1, 6.2 and 6.3, while the intermediate structure Mi is addressed in Section 6.4.

6.1. Effect of the upper mesospheric NO/N ratio on the Mm formation

Three IonA-2 model scenarios are used to investigate the effect of the upper mesospheric NO/N ratio on the Mm formation under constant SIP V2.38 solar flux conditions at the top of the Martian atmosphere. The first row of Fig. 10 contains neutral and ion/electron density profiles calculated with the IonA-2_{flux} scenario, i.e. the photochemical reaction scheme described in Table C1. This results in a dominance of NO over N in the upper mesosphere. The second row contains the convergent results for the IonA-2_{part} scenario, where the limiting velocities at the homopause are reduced to 1% of IonA-2_{flux}, while the reaction rate coefficient of $N + CO_2 \rightarrow NO + CO$ (IR012) is reduced to 4% of the original value (following the discussion of Stevens et al., 2019 concerning the temperature dependence of the reaction rate coefficient).

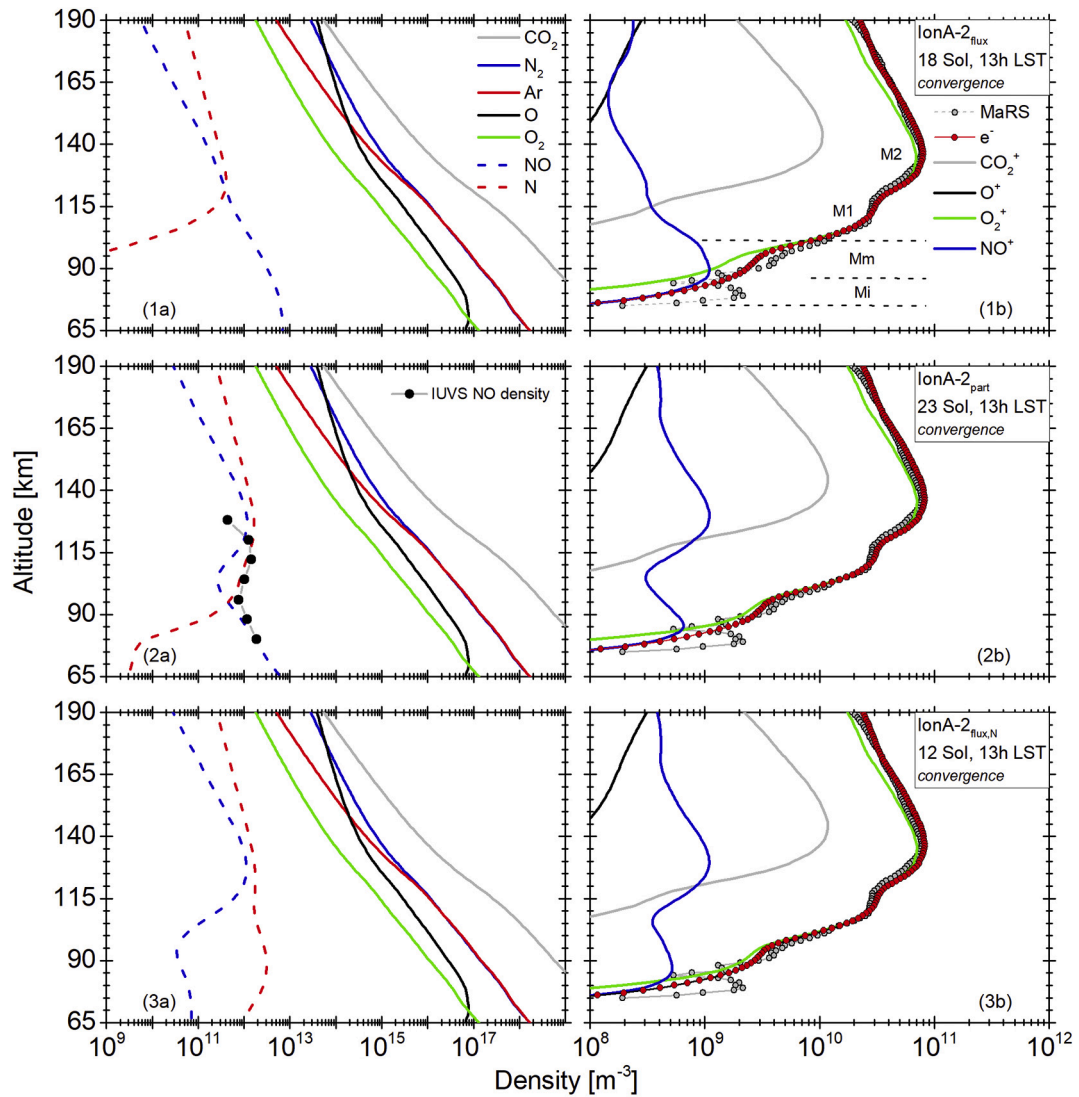


Fig. 10. IonA-2 neutral atmosphere (left column) and ionosphere (right column) for DoY 336 (2005) and solar zenith angle 78.78° for different model scenarios. MaRS ionospheric electron density observations are plotted for comparison. The black dots in Panel 2a indicate the MAVEN IUVS dayglow results (Stevens et al., 2019, Fig. 6) for a pl. latitude of 53° , solar zenith angle of 75° and 18 h local solar time.

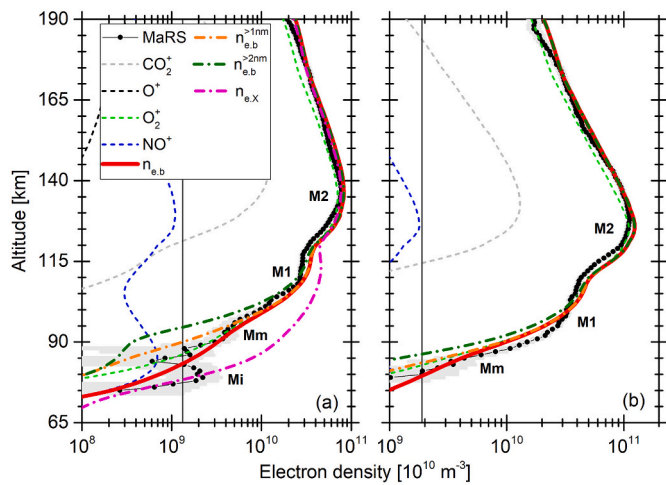


Fig. 11. Ionospheric IonA-2_{part} results $n_{e,b}$ for φ_b solar input flux in comparison with the MaRS observations of (a) DoY 336 (2005) for $\chi = 78.78^\circ$ and Earth-Sun-Mars (ESM) angle of $\sim 11^\circ$ (b) DoY 041 (2006) for $\chi = 54.28^\circ$ and ESM of $\sim 47^\circ$.

The third row of Fig. 10 shows the convergent state of the IonA-2_{flux,N} scenario, where the reaction $N + CO_2 \rightarrow NO + CO$ (IRO12) is disabled.

The modified reaction scheme in the IonA-2_{flux,N} scenario results in a dominance of N over NO in the upper mesosphere.

The merged excess electron density feature occurs in all IonA-2 scenarios without an additional enhancement of the SIP V2.38 X-ray fluxes and does not heavily depend on the NO/N ratio in the upper mesosphere. The modeled Mm are mostly similar in altitude, extent and

density in all model scenarios. Only the ionospheric O_2^+/NO^+ ratio changes with the amount of NO present in the upper mesosphere. All scenarios are in good agreement with the observed Mm. The small-scale Mi structure, however, cannot be reproduced in any of the model scenarios. This will be discussed further in Section 6.4. The ionization of the local planetary atmosphere by solar radiation provides a sufficient explanation for the general occurrence of merged excess electron density in the MaRS observation independently of the locally available amount of NO in the upper mesosphere.

The remote detection of the nitric oxide dayglow (Stevens et al., 2019) by MAVEN-IUVS provides constraints for the NO density in the upper mesosphere on the planetary dayside. The best agreement between the MAVEN-IUVS observation and the IonA-2 model is reached with the IonA-2_{part} scenario (see average MAVEN-IUVS profile in Fig. 10, Panel 2a), where the model NO density and MAVEN-IUVS observation agree within the 1- σ natural variability given in fig. 6 of Stevens et al. (2019). Therefore further investigations are conducted based on the IonA-2_{part} scenario.

6.2. The origin of the merged excess electron densities in IonA-2

Panel (a) and (b) in Fig. 11 compare the IonA-2_{part} results for the approximate times of the MaRS observations on DoY 336 (2005) and DoY 041 (2006) based on the static combined SIP V2.38 and FISM flare V2.0 solar baseline scenarios φ_b for DoY 336 (2005) and DoY 041 (2006) (details about the derivation and calibration procedure in Appendix D). While the results in Fig. 10 contain IonA-2 calculations where SIP V2.38 covers the solar radiation down to 0.45 nm, the applied FISM spectra in Fig. 11 include solar radiation down to 0.2 nm. The Earth-Sun-Mars angles for the selected MaRS observations are small to increase the probability of appropriate input data from the Earth based solar flux

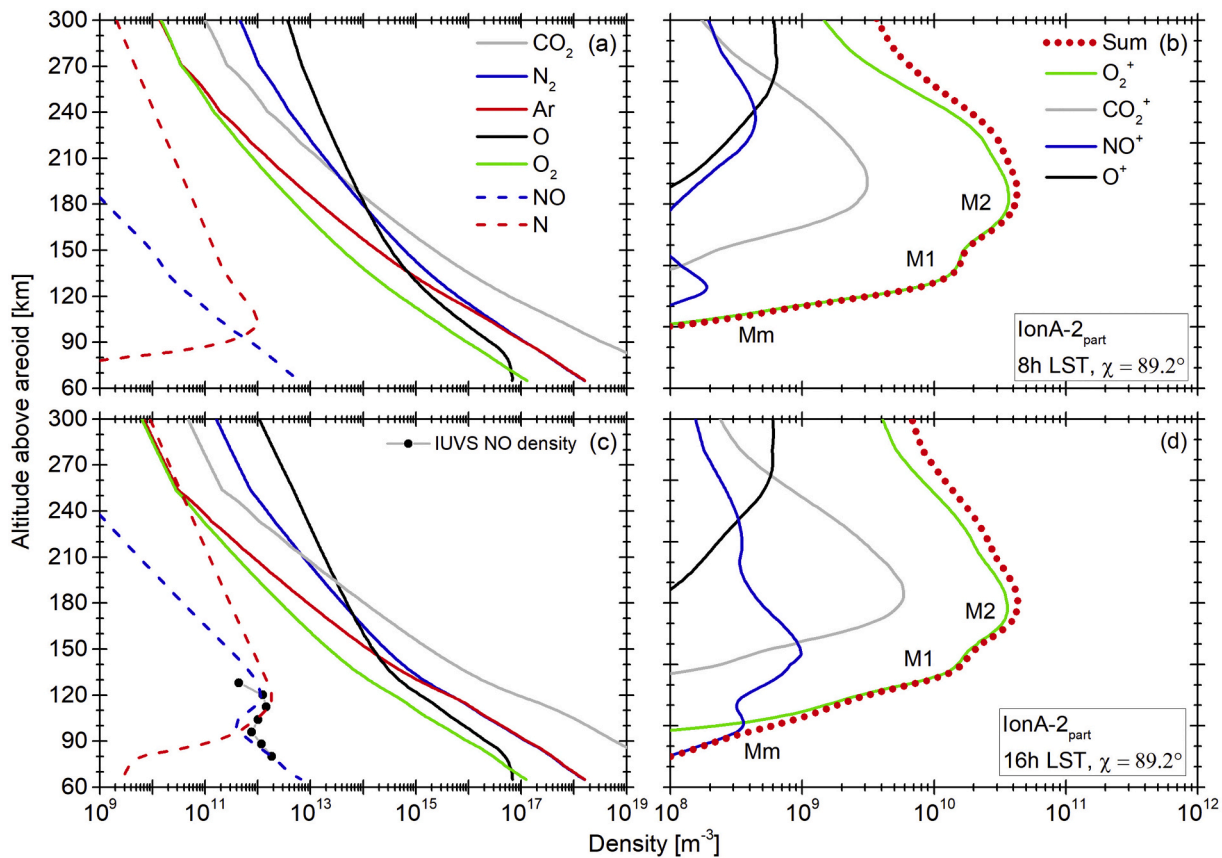


Fig. 12. IonA-2_{part} Martian atmospheric (left column) and ionospheric densities (right column) for 8 h local solar time (top row) and 16 h local solar time (bottom row). Panel (c) also contains the MAVEN-IUVS NO density derived from NO dayglow observations (Stevens et al. 2019). The applied FISM flare V2.0 spectrum is extracted for DoY 336 (2005), 2:24 h.

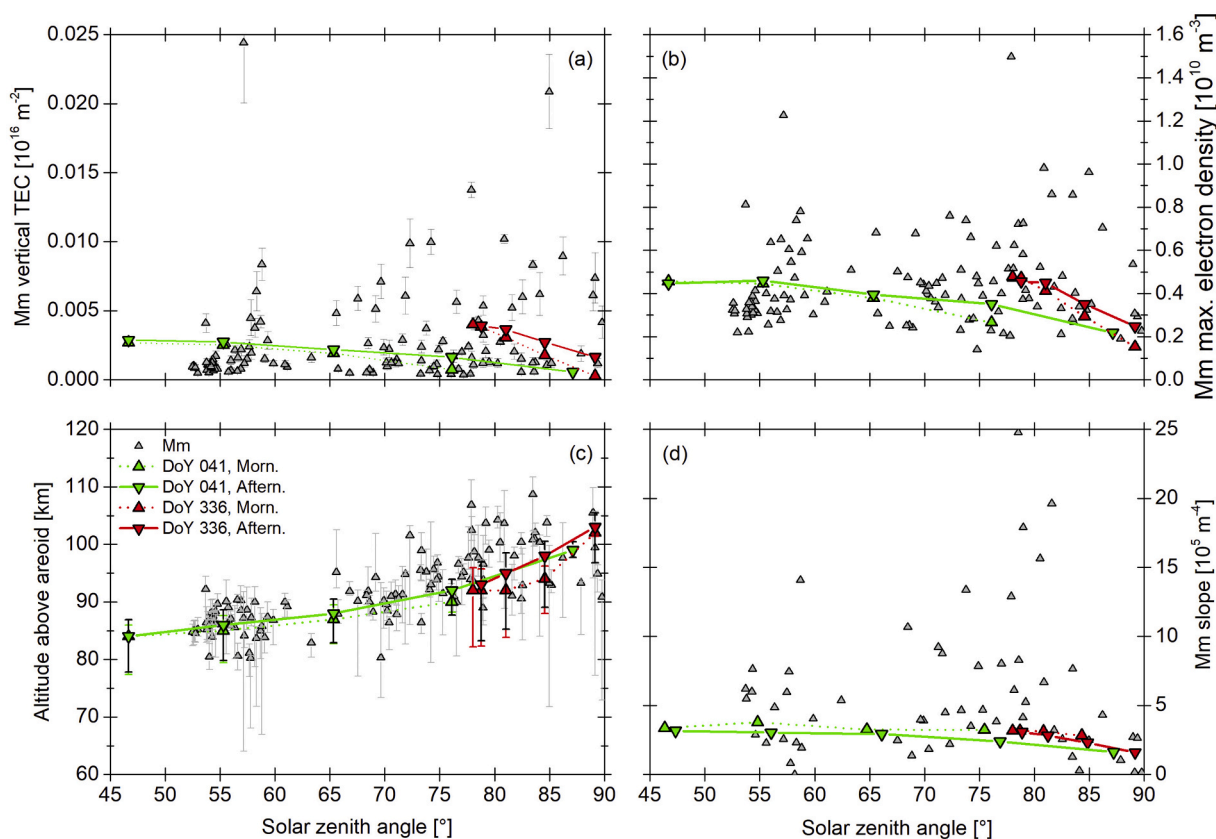


Fig. 13. (a) Vertical TEC, (b) maximum electron density, (c) altitude range and (d) slope of the observed Mm (gray triangles) in comparison with the morning (dashed) and afternoon (solid) IonA-2_{part} results for DoY 336 (2005) (red) and 041 (2006) (green). (For interpretation of the references to colour in this figure legend, the reader is referred to the web version of this article.)

models. While the modeled M2 and M1 peak regions are in good agreement with the observation of DoY 336 (2005) in Fig. 10, the difference between observation and model slightly increases when the φ_b spectrum is applied in Fig. 11a. The modeled Mm are, however, found well within the error bars of the observations. Further model runs are conducted for solar radiation >1 nm ($\varphi_b^{>1nm} \rightarrow n_{e,b}^{>1nm}$) and >2 nm ($\varphi_b^{>2nm} \rightarrow n_{e,b}^{>2nm}$). The comparison between the resulting electron density profiles indicates that removing all solar radiation <1 nm affects mostly the lower Mm region, while removing all solar radiation <2 nm also affects the altitude of the M1 region. The detailed analysis of the derived model Mm parameters in Appendix D confirms these findings.

6.3. The effect of the diurnal cycle on the Mm formation

Fig. 12 illustrates the effect of the diurnal cycle on the Mm formation based on the static combined SIP V2.38 and FISM flare V2.0 solar baseline scenario φ_b . The model solar zenith angles at 8 and 16 h local solar time are equal, which results in similar solar radiation input for both ionospheric profiles at those times. The larger NO^+ densities at e.g. 120 km or 80 km altitude at 16 h local solar time are remnants of the NO^+ accumulation during the day. Until ~ 12 h the NO^+ production by the interaction of O_2^+ with nitrogen species exceeds its loss by (dissociative) recombination, leading to an accumulation of NO^+ . After ~ 12 h the latter process becomes dominant, causing a continuous reduction of NO^+ density during the second half of the day.

Panel (a) to (c) in Fig. 13 illustrate the diurnal variation of the model Mm of DoY 336 (2005) and 041 (2006). The increase in model altitude for increasing solar zenith angles is well in agreement with the observations. The variation of the model Mm slope, peak density and TEC is well within the observed parameter range, but the predicted decrease for increasing solar zenith angle is not seen in the observations. The

predicted trend might be covered in the MaRS observations by a change in atmospheric conditions and/or variations in the short solar X-ray radiation output.

6.4. The effect of flares on the Mm formation

Baseline and solar flare conditions are applied in IonA-2 to investigate which of the observed Mm shapes can be explained by the variability of solar X-ray radiation <2 nm. Fig. 14a illustrates the effect of the temporal variation of the solar radiation below 1 nm on the Martian ionosphere. The IonA-2 atmospheric/ionospheric density start conditions are similar to those used in Fig. 11a. Ionospheric electron densities are computed for distinct time steps with the original solar flux distribution (φ_b), a flux distribution where the short solar X-ray <1 nm is set to zero ($\varphi_{b,red}$) and increased by a factor 10 ($\varphi_{b,incr}$). An increase/decrease in solar fluxes at wavelengths below 1 nm yields a prompt (in minutes) increase/decrease of the Mm density compared to the changes of the original ionosphere induced by the changing solar zenith angle alone. This fast response of the ionosphere to changes in solar X-ray fluxes <1 nm might partially explain the sporadic appearances of the Mm structure in the MaRS observations (behavior for solar X-ray fluxes <2 nm almost similar).

The Panels (b) to (f) of Fig. 14 illustrate the effect of flares on the Martian dayside ionosphere. 1.5 h time sequences of FISM flare V2.0 solar spectra are selected for the [M] flare scenario (09. June 2007, 13:30–15:00, 60s temporal resolution, maximum 1A - 8A integrated flux of $\sim 1.8 \cdot 10^{-5} \text{ W m}^{-2}$ at 13:41 at Earth) and the [X] flare scenario (09. Sept. 2005, 2:09–3:39, 60s temporal resolution, maximum integrated flux of $\sim 2 \cdot 10^{-4} \text{ W m}^{-2}$ at 2:59 at Earth). The calibration of the flare time sequence to the Mars position is summarized in Appendix D. Fig. 14b illustrates the individual baseline [b] and flare [M], [X] solar flux

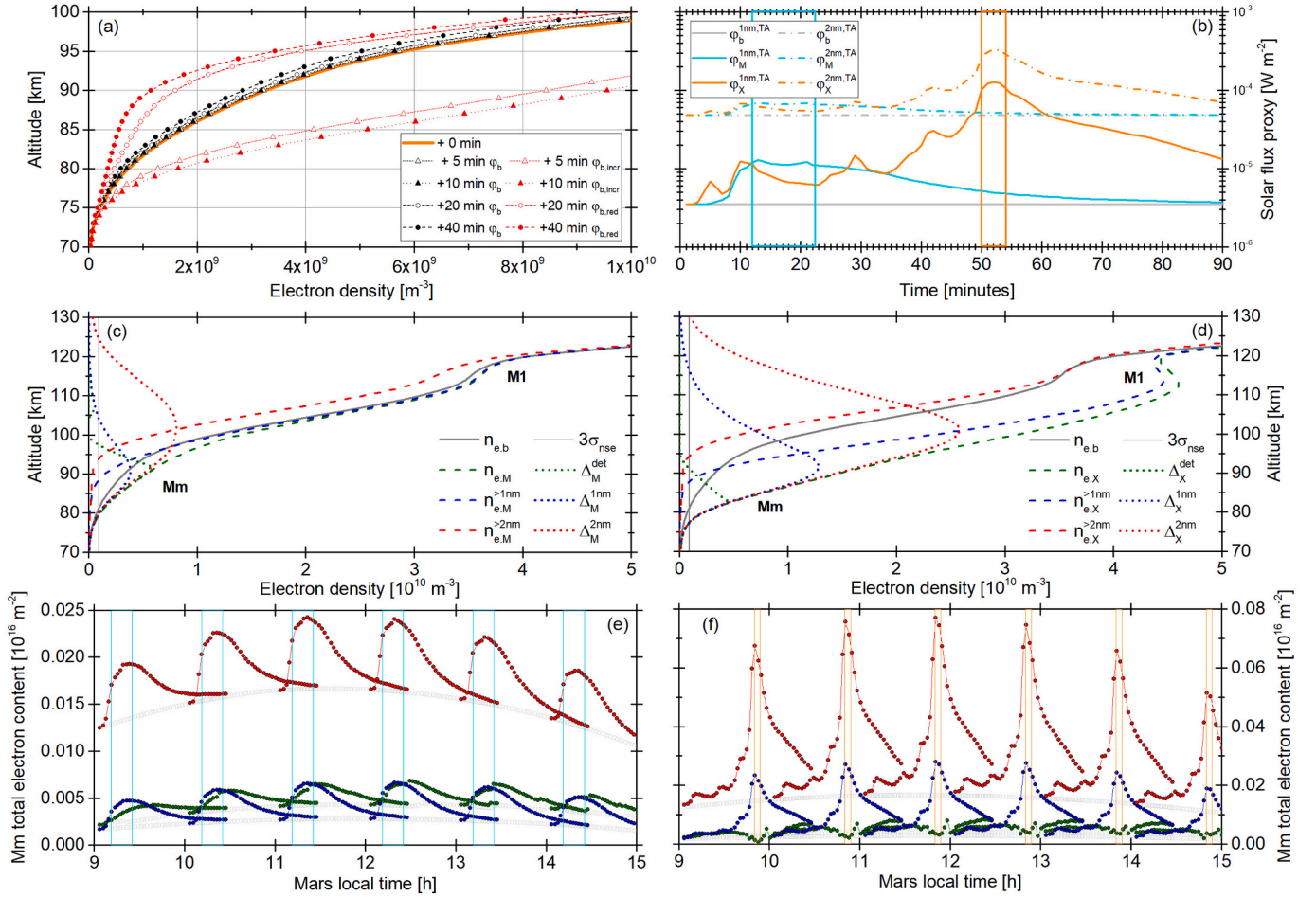


Fig. 14. Variability of the IonA-2 Mm parameters for the MaRS DoY 336 (2005) observation conditions for the baseline ϕ_b and ϕ_M/ϕ_X flare scenarios. (a) Effect of the short time solar radiation variation < 1 nm on the Mm formation. (b) Solar flux proxies for the baseline [b], [M] and [X] flare scenarios at the top of the atmosphere. The light blue and orange rectangles indicate the time range where ϕ_M^* and ϕ_X^* reach their respective maximum. (c) – (d) IonA-2 model electron densities and associated Δ_M^{det} , Δ_M^{1nm} and Δ_M^{2nm} for the 13 h MLST model run where the flare reaches its maximum for flare radiation < 2 nm. (e) – (f) Mm TEC derived from Δ_M^{det} , Δ_M^{1nm} and Δ_M^{2nm} Gray markings indicate the [b] scenario results. The assumed noise level σ_{nse} for the Mm parameter calculations is $3 \cdot 10^8 \text{ m}^{-3}$. The colored rectangles indicate the flare peak time ranges highlighted in (b) for each model run. (For interpretation of the references to colour in this figure legend, the reader is referred to the web version of this article.)

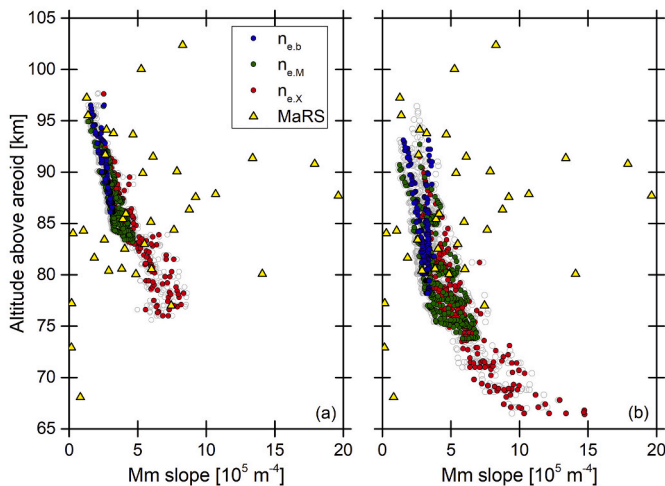


Fig. 15. Comparison of observed (Mm₂ – Mm₅) and model ϕ_b , ϕ_M and ϕ_X α_{Mm} and h_L Mm parameters for (a) DoY 336 (2005) and (b) DoY 041 (2006). Gray circles indicate the model Mm parameters for $\sigma_{nse} = 2.0 \cdot 10^8 \text{ m}^{-3}$ and $\sigma_{nse} = 4.0 \cdot 10^8 \text{ m}^{-3}$.

sequences based on the integrated FISM solar flux between 0.2 and 1 nm ($\phi_{1nm,TA}^*$) and 0.2 and 2 nm ($\phi_{2nm,TA}^*$) at the top of the Mars atmosphere. The solar flux for the [M] flare scenario (ϕ_M) and the [X] flare scenario (ϕ_X) are applied at each Mars hour between 9 h and 15 h MLST. The response of the ionosphere is provided by IonA-2 in 2 min intervals for all solar radiation ($n_{e,*}$), solar radiation > 1 nm ($n_{e,*}^{>1nm}$) and solar radiation > 2 nm ($n_{e,*}^{>2nm}$). The Mm parameters are determined from the detected Mm region Δ_M^{det} , the residual electron densities originating from 1 nm solar radiation ($\Delta_M^{1nm} = n_{e,*} - n_{e,*}^{>1nm}$), and 2 nm radiation ($\Delta_M^{2nm} = n_{e,*} - n_{e,*}^{>2nm}$). The comparison of the [M] flare results with the baseline [b] scenario in Fig. 14c indicates that the flux enhancement in the wavelength range < 1 nm leads to a decrease of the ionospheric base, while the flux enhancement in the wavelength range < 2 nm leads additionally to an enhancement of the M1 regions. The enhancement of the Mm region is reflected in increased Mm TEC (Fig. 14e) and also the Mm peak electron density (Appendix D, Fig. D2). The high energy input during the [X] flare scenario leads to a large altitude decrease of the ionospheric base and an overall enhancement of the M1 region. The altitude range covered by $n_{e,X}$ (see also Fig. 11a) agrees well with the range of the flare enhanced electron density profile observed by MGS in fig. 1 of Mendillo et al. (2006). The applied Mm detection method, however, underestimates the effect of the electron density originating from the solar radiation < 1 and < 2 nm (Fig. 14d, f), except for the slope parameter α_{Mm} and the altitude of the lower Mm boundary h_L .

(Appendix D Figs. D2, D3). α_{Mm} and h_L are therefore used to identify the range of observed Mm reproducible by IonA-2.

While the observed Mm comprise a wide variety of shapes (Table 4), the range of IonA-2 model Mm shapes is in general found to be constraint to smoothly decreasing electron densities below $n_{e,max}(Mm)$ with small δ_{Mm} (opposite to Mm₆, details in Appendix D). At no local time the [b], [M] and [X] scenarios provide Mm with distinct peaks below the M1 base (category Mm₁). While the peak energy <2 nm in the [X] flare scenario provides sufficient ionization energy in the region of interest, no peak structures below M1 occur for any of the applied flare spectra (Fig. 14c, d) at any investigated Mars hour. Also no intermediate structures (Mi, Fig. 11a) are found. The altitude region for the continuous atmospheric absorption region of the individual 1 A solar radiation bins in the model is too wide to produce ionospheric small scale structures without the implementation of further physical processes. Fig. 15 shows the comparison between the observed Mm in the remaining categories Mm₂ to Mm₅ and the derived DoY 336 (2005) and DoY 041 (2006) Mm baseline and flare parameters. Combinations of moderate h_L and α_{Mm} are well reproduced by IonA-2 (e.g. Fig. 11a, b), while Mm with large α_{Mm} (e.g. Figs. 1c, d; 2a) cannot be explained. The combination of low h_L and extremely small slopes is also not covered by the model. Those Mm, however, result from MaRS observations where the electron density of the detected Mm is only slightly larger than $3\sigma_{nse}$ (e.g. Fig. 2c).

7. Summary and conclusions

The MaRS_{quiet} radio science observations allowed the investigation of the lower base region of the Mars dayside ionosphere in unprecedented detail. Merged excess electron density features are identified in approximately 42% of the MaRS_{quiet} data set over the full accessible solar zenith angle range (50° - 90°). The base of the electron density profiles containing Mm is on average found lower in the atmosphere than the base of the averaged undisturbed MaRS profiles. This suggests a dependence of the Mm formation on energy sources which are able to penetrate deep into the atmosphere. This is supported by the strong positive correlation with the Sun's activity proxy $\phi_{\leq 95}^E$, because an increase in solar activity is regularly accompanied by an increase of flares, CMEs and also short solar X-ray and Ly- α fluxes. No correlation is found between P_{Mm} and the individual solar flux proxies, potentially due to the temporal/spatial constraints of the underlying solar flux data set. A wide range of Mm shapes is observed, ranging from smoothly decreasing electron densities to peak structures below the base of M1.

Investigations with the IonA-2 photochemical model for undisturbed and flare conditions show that the ionization of the local neutral atmosphere by solar X-ray radiation <2 nm provides a satisfying explanation for detected Mm features with smoothly decreasing electron density below $n_{e,max}(Mm)$ and moderate α_{Mm} and $h_{L,S}$. While sufficient ionization energy reaches the region of interest in the [X] flare scenario, neither peaks below the M1 base (Mm₁) nor intermediate Mi features occur in the resulting electron density profiles. While previous modeling studies have typically focused on higher altitude regions, the altitude range of the applied models regularly extends to regions where the excess electron densities occur. The 1-D photochemical models of Fox (2009) and Matta et al. (2013) both provide approximate densities of $2 \cdot 10^9 \text{ m}^{-3}$ at an altitude of 80 km with more or less pronounced smooth slope changes at the ionospheric base, indicating the potential presence of a weak Mm region. The diurnal change of the ionospheric base derived from a 3-D general circulation model (Fig. 3, González-Galindo et al. (2013)) is in overall agreement with the IonA-2 results in Fig. 11. However, no pronounced Mm region is present in the shown results. None of the mentioned models contain pronounced Mi or peaks below the M1 base. This is also true for the 1-D photochemical model of Lollo et al. (2012) who investigate the effect of moderate and high energy flares on the dayside ionosphere of Mars. This supports the conclusion that the identified Mi and peaks below the M1 base must have an origin different from the sole variability of solar X-ray radiation during

undisturbed and flare conditions.

An exclusive meteoric origin of the found peak structures below the M1 base is also unlikely. Crismani et al. (2017) use one Mars year of MAVEN-IUVS ultraviolet remote sensing Mg⁺ detections to show its temporal variability in dependence of diurnal fluctuations, Martian seasons, dust storms and potential enlarged particle influx by meteor showers. While the altitude of the detected Mg⁺ layer is in good agreement with the derived Mm altitudes (Fig. 7), the densities observed by MAVEN-IUVS are all below $1 \cdot 10^9 \text{ m}^{-3}$, even during periods of predicted meteor showers. This value is below the current detection limit of merged excess electron density features in MaRS observations (Fig. 8). No supporting effects of the weak crustal magnetic fields were found on the Mm formation.

More likely origins for the identified peak structures (Mm₁), intermediate structures (Mi) and other determined shapes deviating from moderate $\alpha_{Mm}/h_{L,S}$ conditions are local temperature changes during flares, particle precipitation, SEPs, gravity waves, local impact ionization effects from penetrating solar wind ions (Crismani et al., 2019) or the deviation from a radial symmetric ionosphere caused by other effects.

It is indicative from the IonA-2 model results that the general increase/decrease of solar X-ray <2 nm leads to a correlated response of the Mm region. The sporadic presence of the merged excess electron density feature in the MaRS observations is therefore thought to be a combination of observational (increased observation noise level compared to the available amount of X-ray radiation <2 nm, shift of the lower baseline by ionospheric deviations from radial symmetry – which will be discussed in a future publication) and environmental (e.g. solar X-ray variation <2 nm) factors.

Declaration of Competing Interest

None.

Acknowledgments

The Mars Express Radio Science Experiment (MaRS) is funded by the German Space Agency (DLR) under the Grant 50QM1802. Support for Mars Express Radio Science at Stanford University is provided by NASA through a JPL Contract. Support for the Multimission Radio Science Support Team is provided by NASA/JPL. Portions of this research were performed at the Jet Propulsion Laboratory, California Institute of Technology under contract with NASA. We thank everyone involved in the Mars Express project at ESTEC, ESOC, ESAC, JPL, and the ESTRACK and DSN ground stations for their continuous support.

K. P. and M. P. acknowledge funding for this project by the Deutsche Forschungsgemeinschaft (DFG) under Grant PA 525/11-1, PA525/11-2 and PA 525/14-1.

F.G.G. is funded by the Spanish Ministerio de Ciencia, Innovación y Universidades, the Agencia Estatal de Investigación and EC FEDER funds under project RTI2018-100920-J-I00, and acknowledges financial support from the State Agency for Research of the Spanish MCIU through the "Center of Excellence Severo Ochoa" award to the Instituto de Astrofísica de Andalucía (SEV-2017-0709).

Solar Irradiance Platform historical irradiances are provided courtesy of W. Kent Tobiska and Space Environment Technologies. These historical irradiances have been developed with partial funding from the NASA UARS, TIMED, and SOHO missions.

We acknowledge support for work conducted on the development of the Mars Climate Database from the European Space Agency (under ESTEC Contract 11369/95/NL/JG(SC)) and from CNES. CNRS (LMD group), the IAA and the UK Particle Physics and Astronomy Research Council (AOPP, Oxford Group) also provided support during the development of the Martian General Circulation Models.

We thank the NAIF-team at JPL (headed by Charles Acton) for providing the SPICE software.

We also like to thank the reviewers for their valuable reviews and constructive suggestions.

Appendix A. The lowest valid altitude of the ionospheric electron density $h_{L, \text{val}}$ in radio science observations

The lowest valid altitude of the ionospheric electron density $h_{L, \text{val}}$ is defined as that altitude where the neutral atmosphere is strong enough to bias the observation of the ionospheric electron density. For the MaRS observations illustrated in Fig. 1, the electron density derived from differential Doppler (n_e^D) stays close to the zero line below the M1 layer while the electron density derived from X-Band (n_e^X) becomes increasingly negative below ~ 80 km altitude. This different behavior of n_e^X and n_e^D is caused by dispersion (Pätzold et al., 2009, 2016). The radio ray is refracted by a combination of the ionospheric (N_e) and the neutral atmospheric (N_n) refractivities. While N_e is frequency dependent, N_n is approximately not. Due to the opposite signs of N_e and N_n , n_e^X gets increasingly negative when N_n starts to dominate. This is not the case for n_e^D . When N_n dominates, the received Doppler shift at the ground station for X-band $\Delta f_{GS, X}$ and S-band $\Delta f_{GS, S}$ should be equal and Eq. (1) in the original paper causes only a small negative drift of the differential Doppler. It is expected, that n_e^D is zero below the ionospheric base only, when (i.) no deviations from a radially symmetric ionosphere occur, (ii.) the neutral atmosphere is not yet strong enough to affect the radio ray, (iii.) no other error sources (e.g. additional plasma in the radio ray) are present and (iv.) the atmospheric path differences between the X- and S-band radio rays are not large yet, so that similar regions of the atmosphere are sounded. This discussion shows, that n_e^X and n_e^D are only useful above a certain altitude. Below that altitude, n_e^X becomes increasingly negative, while n_e^D is valid only until N_n dominates the refraction process or other sources bias the observation. The lowest valid altitude $h_{L, \text{val}}$ is therefore determined from n_e^X . It is chosen to be that altitude below the ionospheric main peak at which the negative electron density exceeds $-3\sigma_{nse}$ for the last time. It is assumed here that below this altitude the effect of the neutral atmosphere on the radio ray is potentially strong enough to bias the n_e^D profiles.

Appendix B. Automated procedure for the determination of the M1 and Mm characteristics

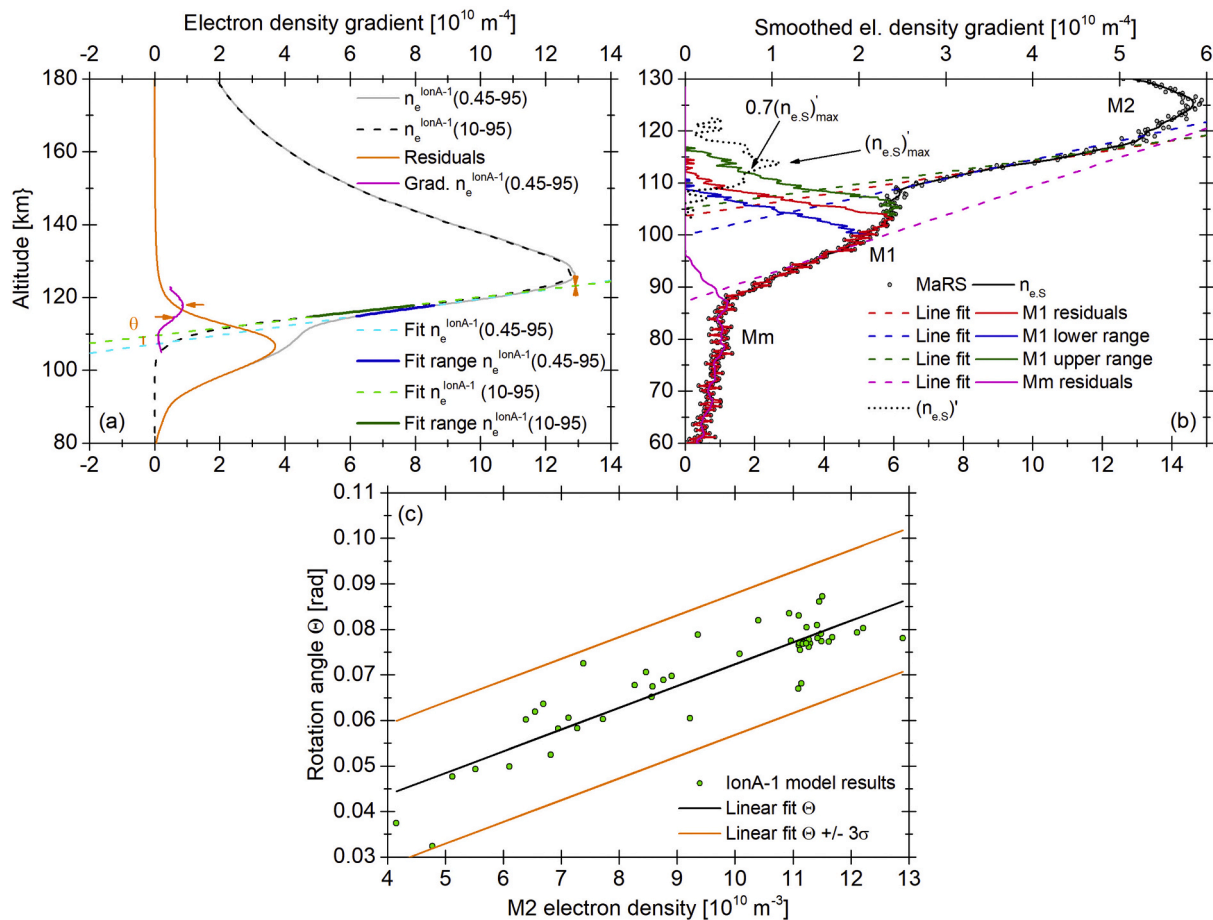


Fig. B1. (a) IonA-1 results for the MaRS observation of DoY 263 (2009), $L_S = 341.59^\circ$, $\text{lon} = 159.30^\circ$, $\text{lat} = -19.82^\circ$, $\chi = 51.01^\circ$. The purple line is the gradient of $n_e^{\text{IonA-1}}(0.45-95)$. The dashed blue line is the fit on the dark blue part of $n_e^{\text{IonA-1}}(0.45-95)$, the dashed green line the fit on the dark green part of $n_e^{\text{IonA-1}}(10-95)$. The orange arrows indicate the altitude range for the $n_e^{\text{IonA-1}}(0.45-95)$ line fit. The orange triangles indicate the projected M2 maximum electron density on the $n_e^{\text{IonA-1}}(0.45-95)$ line fit. θ is the rotation angle between both line fits. (b) M1 and Mm parameter determination for the MaRS observation of DoY 337 (2013), $L_S = 57.59^\circ$, $\text{lon} = 56.99^\circ$, $\text{lat} = 17.69^\circ$, $\chi = 57.16^\circ$. Gray circles show the original MaRS data. The black line indicates the smoothed observation, while the black dotted line illustrates the gradient of the smoothed MaRS observation. Red, blue and green lines indicate the electron density residuals for the M1 parameter determination with lower and upper ranges. The residuals are determined from the associated line fits (dashed lines). Magenta lines indicate the Mm residuals and line fit. Further descriptions of the M1 parameter determination are found in the text. (c) θ for the 50 modeled MaRS observations (Figure adapted from Peter (2018)). (For interpretation of the references to colour in this figure legend, the reader is referred to the web version of this article.)

B.1. Derivation of the M1 characteristics

An automated procedure is applied to the MaRS_{quiet} data set to derive the M1 characteristics for all observations.

- Data smoothing

The determination of the M1 characteristics depends on the first derivation of the electron density profiles. Misdetections are avoided by removing the small scale noise in the MaRS electron density profiles by repetitive smoothing with a short window moving average of each individual MaRS profile until its noise level falls below $\sigma_{nse,L} + 1.0 \cdot 10^7 m^{-3}$. This yields the smoothed electron density profiles $n_{e,S}$.

- M1 parameter determination

The M1 characteristics are derived from the n_e residuals after a straight line fit on the base of the M2 region. The altitude region for this fit is determined from the gradient of the smoothed electron densities $\frac{dn_e}{dh} = (n_{e,S})'$. Fig. B1 illustrates that an ideal/undisturbed two-layered ionospheric structure yields a sinus-shaped gradient below the M2 layer with a maximum between M2 and M1. The minimum of the gradient indicates the presence of M1. The altitude range for the line fit in the MaRS observation is determined from those altitudes where $(n_{e,S})'$ (dotted line in Fig. B1(b)) is found between the gradient maximum $(n_{e,S})'_{max}$ and $0.7 \cdot (n_{e,S})'_{max}$. The straight line fit (red dashed line) is then applied on n_e in the identified altitude range. The M1 parameters are derived from the calculated residuals (red straight line) with algorithms similar to that used for the determination of the M2 parameters.

- M1 lower and upper range approximation

Lower and upper ranges of the M1 parameters are given as an estimate for the uncertainties introduced by the application of the straight line fit method. The lower range of the M1 parameters is determined by a method similar to that applied for the M1 parameter determination. The fit altitude range is determined by the gradient range of $0.85 \cdot (n_{e,S})'_{max}$ to $0.4 \cdot (n_{e,S})'_{max}$. These new boundaries yield a closer line fit to the base of M2, thereby potentially removing a small part of M1. This results in smaller electron density residuals for the lower M1 range approximation.

The upper range of the M1 parameters is determined by rotating the center line fit around the projection of $n_{e,max}(M2)$ (indicated by orange triangles in Fig. B1(a)) by an angle of

$$\Theta(n_{e,max}(M2)) = 4.8 \cdot 10^{-13} [m^{-3}] \cdot n_{e,max}(M2) + 0.0246 [rad] + 3\sigma \quad (B1)$$

$$\sigma = 0.0052 [rad]$$

The derived straight line is then subtracted from n_e and the M1 upper range parameters are derived from the residuals.

Eq. (B1) was derived from a selection of 50 MaRS observations (Fig. B1(c)), which have been modeled with the 1-D photochemical equilibrium model IonA-1 (Peter et al., 2014) using the SIP V2.38 solar flux (Tobiska et al., 2000) and the Mars Climate Database V5.2 neutral atmosphere (Lewis et al., 1999; Millour et al., 2015). The IonA-1 electron densities were calculated by using solar radiation up to 95 nm ($n_e^{IonA-1}(0.45-95)$) and solar radiation from 10 nm to 95 nm ($n_e^{IonA-1}(10-95)$). While the obtained $n_e^{IonA-1}(0.45-95)$ profiles contain a pronounced M1 region, the $n_e^{IonA-1}(10-95)$ profiles show a complete lack of the M1 layer. In addition, the lower ionospheric base of $n_e^{IonA-1}(10-95)$ is slightly shifted to higher altitudes compared to the base of $n_e^{IonA-1}(0.45-95)$. This indicates, that a fit on the M2 baseline also removes a small part of the M1 layer. This effect has been estimated by determining the rotation angles between the two fitted straight lines on $n_e^{IonA-1}(0.45-95)$ and $n_e^{IonA-1}(10-95)$ for the 50 selected MaRS observations. Eq. (B1) is a linear regression on the derived rotation angles θ and σ is the error of the slope (see Fig. B1(c)). A detailed analysis of this method is found in Peter (2018), where the test results have also been used to validate the described method for the M1 center parameters as well as their upper and lower ranges. For that, the derived model M1 parameters are compared with the characteristics of the “real” model results, which are determined by subtracting $n_e^{IonA-1}(10-95)$ from $n_e^{IonA-1}(0.45-95)$. It was found that the $n_{e,max}(M1)$ and $h_{max}(M1)$ parameters derived with the aforementioned method are in good agreement with the “real” model results. The $n_{TEC}(M1)$ is obtained within the given parameter boundaries, although slightly underestimated.

B.2. Derivation of the Mm characteristics

The method applied for the parameter derivation of the merged excess electron densities is similar to that used for the derivation of the M1 characteristics. A new gradient maximum $(n_{e,S})'_{max}$ is determined below $h_{max}(M1)$ and the straight line fit is conducted within the altitude range where the gradient reaches $(n_{e,S})'_{max}$ to $0.7 \cdot (n_{e,S})'_{max}$. The Mm vertical TEC $n_{TEC}(Mm)$, peak electron density $n_{e,max}(Mm)$, peak altitude $h_{max}(Mm)$, lower $h_{L,S}$ and upper extent $h_{U,S}$ are then derived from the smoothed residuals. $h_{U,S}$ and $h_{L,S}$ are those altitudes where the smoothed residual electron density falls below $3 \sigma_{nse}$ above and below $h_{max}(Mm)$. The slope of the lower Mm region α_{Mm} is determined from a straight line fit on $n_{e,S}$ between $h_{L,S}$ and $h_{max}(Mm)$ - 0.5 km.

Appendix C. The IonA-2 model

IonA-2 (Ionization in Atmospheres - 2) is a time-marching photochemical transport model with an implemented diurnal cycle. IonA-2 solves the system of 1-D continuity equations

$$\frac{\partial n_s}{\partial t} + \frac{\partial}{\partial z}(n_s w_s) = P_s^{tot} - L_s^{tot} \quad (C1)$$

for each species s simultaneously. n_s is the number density, w_s is the velocity, P_s^{tot} is the total photochemical production and L_s^{tot} the total photochemical loss of species s , t is the time variable and z is the vertical direction. Eq. (C1) is solved by applying the operator splitting method (Jacobson, 2007), where the transport and the photochemistry parts of the continuity equation are solved in a sequential manner for each time step. The photochemical reaction scheme is listed in Table C1. The system of stiff ordinary differential equations is solved with the Matlab ODE15s solver, which is based on the semi-implicit Gear's method (Gear, 1971; Jacobson, 2007). A summary of the model parameters is given in Table 5 of the paper.

The 1-D minor molecular diffusion equation implemented in IonA-2 is described in [Banks and Kockarts \(1973\)](#).

$$n_s w_s = - (K + D_s^m) \frac{\partial n_s}{\partial z} - n_s \left[K \left(\frac{\langle m \rangle g}{k_B T_N} + \frac{1}{T_N} \frac{\partial T_N}{\partial z} \right) + D_s^m \left(\frac{m_s g}{k_B T_s} + \frac{1 + \beta_{corr}}{T_s} \frac{\partial T_s}{\partial z} \right) \right], \quad (C2)$$

where K is the eddy diffusion coefficient, D_s^m the molecular diffusion coefficient, g the gravity acceleration and k_B the Boltzmann constant. T_N and T_s are the average neutral and individual species temperature, respectively. β_{corr} is a correction factor, which accounts for thermal diffusion of light species ([Colegrove et al., 1966](#)). β_{corr} is set to -0.25 for H and H₂ and to zero otherwise in IonA-2. $\langle m \rangle = \sum_s n_s m_s / n_N$ is the average atmospheric mass, where m_s is the mass of species s and n_N is the neutral atmospheric number density. It is assumed that $T_N = T_s$ for all neutral species in IonA-2.

The eddy diffusion coefficient K is derived from the expression

$$K(z) = 1.4 \cdot 10^{13} (n_N(z))^{-0.5}, \quad (C3)$$

following the discussion in [Krasnopolsky \(1986\)](#) and [von Zahn et al. \(1980\)](#). The minor molecular diffusion coefficient D_s^m for the diffusion of species s through other gases u is calculated following [Colegrove et al. \(1966\)](#).

$$D_s^m = \frac{\sum_u n_u}{\sum_{u \neq s} \frac{n_u}{D_{su}^b}}, \quad (C4)$$

where D_{su}^b is the binary diffusion coefficient, which is calculated from ([Poling et al., 2001](#); [Chapman and Cowling, 1939](#))

$$D_{su}^b = \frac{3}{16} \frac{(2\pi k_B T_N / M_{su})^{1/2}}{n \pi \sigma_{su}^2 \Omega_D} f_D, \quad (C5)$$

where $M_{su} = M_s \cdot M_u / (M_s + M_u)$ is the reduced molecular/atomic weight of species s and u , M_s and M_u are the associated molecular/atomic weights. n is the number density of molecules/atoms in the mixture, σ_{su} is the characteristic length of the intermolecular force law between s and u . f_D is a molecular diffusion correction term and assumed to be equal to 1 for the IonA-2 calculations. Ω_D is the collision integral for diffusion, which is described in IonA-2 by the 12–6 Lennard-Jones potential ([Poling et al., 2001](#); [Neufeld et al., 1972](#)).

Major ambipolar diffusion for each ion i is implemented in IonA-2 by (e.g. [Schunk and Nagy, 2009](#))

$$n_i w_i = - D_i^a \left[\frac{\partial n_i}{\partial z} + n_i \left(\frac{m_i g}{2k_B T_p} + \frac{1}{T_p} \frac{\partial T_p}{\partial z} \right) \right], \quad (C6)$$

where D_i^a is the ambipolar diffusion coefficient for ion i and $T_p = (T_i + T_e)/2$ is the plasma temperature. D_i^a is derived from the expression

$$D_i^a = \frac{2k_B T_p}{m_i \nu_i^{coll}}. \quad (C7)$$

The collision frequency ν_i^{coll} for ion i is assumed to be the sum of the neutral-ion ν_i^{in} , ion-ion ν_i^{ii} and ion-electron ν_i^{ie} collision frequencies. The elastic ion-neutral collision frequency ν_i^{in} for ion i is derived from Maxwell molecule collisions ([Banks and Kockarts, 1973](#))

$$\nu_i^{in} = \sum_n \frac{m_n}{m_n + m_i} 2.6 \cdot 10^{-9} n_n \sqrt{\frac{\alpha_n^{pol}}{m_{red}}}, \quad (C8)$$

where n is the atmospheric neutral species, n_n is the neutral number density of species n in units of [cm^{-3}], α_n^{pol} is the polarizability of the neutral species n in [$10^{-24} cm^3$] and $m_{red} = (m_i m_n) / (m_i + m_n)$ the reduced mass in units of atomic masses amu .

The average ion-ion collision frequency for momentum transfer ν_i^{ii} is derived from Coulomb interactions between the ions ([Banks and Kockarts, 1973](#); [Schunk and Nagy, 2009](#))

$$\nu_i^{ii} = \sum_j \frac{m_j}{m_i + m_j} \frac{16\sqrt{\pi}}{3} \frac{n_j m_j}{m_i + m_j} \left(\frac{2k_B T_{red}}{m_{red}} \right)^{-3/2} \frac{q_i^2 q_j^2}{m_{red}^2} \ln(\Lambda) \quad (C9)$$

The masses of the ion species m_i and m_j , n_j and k_B are in gcs units. The Coulomb logarithm $\ln(\Lambda)$ in IonA-2 is assumed to be 15 ([Schunk and Nagy, 2009](#)). q_i and q_e are the ion and electron charges in esu . m_{red} is the reduced mass in [g] and $T_{red} = (m_i T_j + m_j T_i) / (m_i + m_j)$ is the reduced temperature in [K].

The average ion-electron collision frequency for momentum transfer ν_i^{ie} is implemented in IonA-2 as ([Banks and Kockarts, 1973](#))

$$\nu_i^{ie} = \frac{4\sqrt{2\pi}}{3} \left(\frac{n_i q_e^4}{(k_B T_e)^{3/2} \sqrt{m_e}} \right) \ln(\Lambda), \quad (C10)$$

where the ion density n_i is in [cm^{-3}], the electron mass m_e is in [g] and the electron charge q_e is in esu .

The minor molecular diffusion and ambipolar diffusion equations are solved with the implicit and stable numerical method described in appendix O of [Schunk and Nagy \(2009\)](#). The upper flux boundary conditions of molecular diffusion are set to zero for all minor neutral species, the lower flux boundary conditions are set according to the IonA-2 scenario described in [Table 5](#).

The simulation of the diurnal cycle in IonA-2 uses the MCD V5.2 primary neutral species and neutral temperature for a full Martian Sol derived at the planetary longitude and latitude of the modeled MaRS observation in combination with the associated SIP V2.38 solar flux spectrum. The MCD

primary neutral species (Table 5 of the paper), neutral temperature and photoionization calculated from solar radiation are updated every model time step based on the current planetary local time and solar zenith angle. The photochemical scheme in combination with eddy and minor neutral molecular diffusion and ambipolar diffusion of the ions provides vertical profiles of several secondary neutral species (C, H₂O₂, HO₂, O(¹D), N(²D), N, NO, NO₂ and OH) and ions (Ar⁺, CO₂⁺, CO⁺, C⁺, HCO₂⁺, HCO⁺, H⁺, N₂⁺, NO⁺, N⁺, O₂⁺ and O⁺) for a full Martian Sol (see Peter (2018) for further model details). Due to the changing input conditions over one Sol, the model convergence cannot be measured from one time step to the next. The convergence of IonA-2 is therefore tested at a pre-defined local solar time. If the maximum change of the N, N(²D) and NO densities at each altitude falls below 3.5% from one Sol to the next it is assumed that the model has reached convergence.

Table C1

Photochemical reaction scheme for IonA-2.

Number	Reaction	Source
IP001	CO ₂ + hν → CO + O	
IP002	CO ₂ + hν → CO + O(¹ D)	
IP003	H ₂ + hν → H + H	
IP004	H ₂ O + hν → H + OH	
IP005	H ₂ O ₂ + hν → OH + OH	
IP006	N ₂ + hν → N + N(² D)	
IP007	NO + hν → N + O	
IP008	NO ₂ + hν → NO + O	
IP009	O ₂ + hν → CO + O	
IP010	O ₂ + hν → O + O(¹ D)	
IP011	O ₃ + hν → O + O ₂	
IP012	O ₂ + hν → O(¹ D) + O ₂	
IP013	CO + hν → CO ⁺ + e ⁻	
IP014	CO + hν → C ⁺ + O + e ⁻	
IP015	CO + hν → O ⁺ + C + e ⁻	
IP016	CO ₂ + hν → CO ₂ ⁺ + e ⁻	
IP017	CO ₂ + hν → O ⁺ + CO + e ⁻	
IP018	CO ₂ + hν → CO ⁺ + O + e ⁻	
IP019	CO ₂ + hν → C ⁺ + O ₂ + e ⁻	
IP020	H + hν → H ⁺ + e ⁻	
IP021	N + hν → N ⁺ + e ⁻	
IP022	NO + hν → NO ⁺ + e ⁻	
IP023	N ₂ + hν → N ₂ ⁺ + e ⁻	
IP024	N ₂ + hν → N ⁺ + N + e ⁻	
IP025	O + hν → O ⁺ + e ⁻	
IP026	O ₂ + hν → O ₂ ⁺ + e ⁻	
IP027	Ar + hν → Ar ⁺ + e ⁻	
IR001	C + CO ₂ → CO + CO	Fox and Sung (2001), estimate
IR002	C + NO → CO + N	Chastaing et al. (2000), branching from Fox and Sung (2001)
IR003	C + O ₂ → CO + O	Chastaing et al. (2000)
IR004	CO + OH → CO ₂ + H	Sander et al. (2011)
IR005	H + H + CO ₂ → H ₂ + CO ₂	Fox and Sung (2001), large uncertainty
IR006	H + HO ₂ → H ₂ + O ₂	Burkholder et al. (2015)
IR007	H + HO ₂ → OH + OH	Burkholder et al. (2015)
IR008	H + HO ₂ → O + H ₂ O	Burkholder et al. (2015)
IR009	H + NO ₂ → NO + OH	Burkholder et al. (2015)
IR010	H + O ₂ → HO ₂	Burkholder et al. (2015)
IR011	HO ₂ + HO ₂ → H ₂ O ₂ + O ₂	Burkholder et al. (2015)
IR012	N + CO ₂ → NO + CO	Fox and Sung (2001), estimate
IR013	N + HO ₂ → NO + OH	Brune et al. (1983)
IR014	N + NO → N ₂ + O	Burkholder et al. (2015)
IR015	N + OH → NO + H	Atkinson et al. (1989)
IR016	N + O → NO	Du and Dalgarno (1990)
IR017	N + O ₂ → NO + O	Burkholder et al. (2015)
IR018	N + O ₃ → NO + O ₂	Burkholder et al. (2015), upper limit
IR019	N(² D) + CO ₂ → NO + CO	Herron (1999)
IR020	N(² D) + O → N + O	Fell et al. (1990)
IR021	N(² D) + N ₂ → N + N ₂	Herron (1999)
IR022	N ₂ + O(¹ D) → N ₂ + O	Burkholder et al. (2015)
IR023	NO + HO ₂ → NO ₂ + OH	Burkholder et al. (2015)
IR024	NO + O ₃ → NO ₂ + O ₂	Burkholder et al. (2015)
IR025	O + HO ₂ → OH + O ₂	Burkholder et al. (2015)
IR026	O + O + CO ₂ → O ₂ + CO ₂	Tsang and Hampson (1986), upper limit
IR027	O + OH → O ₂ + H	Burkholder et al. (2015)
IR028	O + O ₂ + CO ₂ → O ₃ + CO ₂	Burkholder et al. (2015)
IR029	O + NO → NO ₂	Burkholder et al. (2015)
IR030	O + NO ₂ → NO + O ₂	Burkholder et al. (2015)
IR031	O(¹ D) + CO ₂ → O + CO ₂	Burkholder et al. (2015)
IR032	O(¹ D) + H ₂ → H + OH	Burkholder et al. (2015)
IR033	O(¹ D) + H ₂ O → OH + OH	Burkholder et al. (2015)
IR034	O(¹ D) + O ₂ → O + O ₂	Burkholder et al. (2015)
IR035	O ₃ + H → OH + O ₂	Burkholder et al. (2015)
IR036	O ₃ + HO ₂ → OH + O ₂ + O ₂	Burkholder et al. (2015)

(continued on next page)

Table C1 (continued)

Number	Reaction	Source
IR037	$O_3 + OH \rightarrow HO_2 + O_2$	Burkholder et al. (2015)
IR038	$OH + H_2 \rightarrow H + H_2O$	Burkholder et al. (2015)
IP039	$OH + H_2O_2 \rightarrow H_2O + HO_2$	Burkholder et al. (2015)
IP040	$OH + HO_2 \rightarrow O_2 + H_2O$	Burkholder et al. (2015)
IP041	$Ar^+ + CO \rightarrow CO^+ + Ar$	Fox and Sung (2001)
IP042	$Ar^+ + CO_2 \rightarrow CO_2^+ + Ar$	Dotan et al. (1999)
IP043	$Ar^+ + N_2 \rightarrow N_2^+ + Ar$	Fox and Sung (2001)
IR044	$Ar^+ + NO \rightarrow Ar + NO^+$	Anicich (2003)
IR045	$Ar^+ + O_2 \rightarrow Ar + O_2^+$	Fox and Sung (2001)
IR046	$C^+ + CO_2 \rightarrow CO^+ + CO$	Fahey et al. (1981)
IR047	$C^+ + NO \rightarrow NO^+ + C$	Fox and Sung (2001)
IR048	$C^+ + O_2 \rightarrow O^+ + CO$	Anicich (2003)
IR049	$C^+ + O_2 \rightarrow CO^+ + O$	Anicich (2003)
IR050	$CO^+ + CO_2 \rightarrow CO_2^+ + CO$	Anicich (2003)
IR051	$CO^+ + e^- \rightarrow C + O$	Fox and Sung (2001)
IR052	$CO^+ + e^- \rightarrow C + O(^1D)$	Fox and Sung (2001)
IR053	$CO^+ + H \rightarrow H^+ + CO$	Scott et al. (1997)
IR054	$CO^+ + H_2 \rightarrow HCO^+ + H$	Scott et al. (1997)
IR055	$CO^+ + N \rightarrow NO^+ + C$	Scott et al. (1997)
IR056	$CO^+ + NO \rightarrow CO + NO^+$	Anicich (2003)
IR057	$CO^+ + O \rightarrow O^+ + CO$	Anicich (2003), estimated error of 50%
IR058	$CO^+ + O_2 \rightarrow O_2^+ + CO$	Fox and Sung (2001)
IR059	$CO_2^+ + e^- \rightarrow CO + O$	Viggiano et al. (2005)
IR060	$CO_2^+ + H \rightarrow HCO^+ + O$	Borodi et al. (2009)
IR061	$CO_2^+ + H \rightarrow H^+ + CO_2$	Fox (2015)
IR062	$CO_2^+ + H_2 \rightarrow HCO_2^+ + H$	Borodi et al. (2009)
IR063	$CO_2^+ + N \rightarrow CO^+ + NO$	Scott et al. (1998)
IR064	$CO_2^+ + N(^2D) \rightarrow N^+ + CO_2$	Fox and Sung (2001), estimate
IR065	$CO_2^+ + NO \rightarrow NO^+ + CO_2$	Anicich (2003)
IR066	$CO_2^+ + O \rightarrow O_2^+ + CO$	Fehsenfeld et al. (1970), Fehsenfeld and Ferguson (1972)
IR067	$CO_2^+ + O \rightarrow O^+ + CO_2$	Fehsenfeld et al. (1970), Fehsenfeld and Ferguson (1972)
IR068	$CO_2^+ + O_2 \rightarrow O_2^+ + CO_2$	Fox and Sung (2001)
IR069	$H^+ + CO_2 \rightarrow HCO^+ + O$	Anicich (2003)
IR070	$H^+ + O \rightarrow O^+ + H$	Stancil et al. (1999)
IR071	$H^+ + O_2 \rightarrow O_2^+ + H$	Anicich (2003)
IR072	$H^+ + NO \rightarrow H + NO^+$	Anicich (2003)
IR073	$HCO^+ + e^- \rightarrow CO + H$	Fox (2015)
IR074	$HCO_2^+ + CO \rightarrow HCO^+ + CO_2$	Prasad and Huntress Jr (1980), estimate
IR075	$HCO_2^+ + e^- \rightarrow H + O + CO$	Geppert et al. (2004), Gougousi et al. (1997)
IR076	$HCO_2^+ + e^- \rightarrow H + CO_2$	Geppert et al. (2004), Gougousi et al. (1997)
IR077	$HCO_2^+ + e^- \rightarrow OH + CO$	Geppert et al. (2004), Gougousi et al. (1997)
IR078	$HCO_2^+ + O \rightarrow HCO^+ + O_2$	Fox (2015), Langevin estimate
IR079	$N^+ + CO \rightarrow NO^+ + C$	Fox and Sung (2001)
IR080	$N^+ + CO \rightarrow CO^+ + N$	Fox and Sung (2001)
IR081	$N^+ + CO \rightarrow C^+ + NO$	Fox and Sung (2001)
IR082	$N^+ + CO_2 \rightarrow CO^+ + NO$	Anicich (2003)
IR083	$N^+ + CO_2 \rightarrow CO_2^+ + N$	Anicich (2003)
IR084	$N^+ + NO \rightarrow N + NO^+$	Fox and Sung (2001)
IR085	$N^+ + NO \rightarrow N_2^+ + O$	Fox and Sung (2001)
IR086	$N^+ + O \rightarrow N + O^+$	Constantinides et al. (1979), Bates (1989), theoretical estimate
IR087	$N^+ + O_2 \rightarrow O_2^+ + N$	Viggiano et al. (2003), Fox and Sung (2001), Dotan et al. (1997), O'Keefe et al. (1986)
IR088	$N^+ + O_2 \rightarrow O_2^+ + N(^2D)$	Viggiano et al. (2003), Fox and Sung (2001), Dotan et al. (1997), O'Keefe et al. (1986)
IR089	$N^+ + O_2 \rightarrow NO^+ + O$	Viggiano et al. (2003), Fox and Sung (2001), Dotan et al. (1997), O'Keefe et al. (1986)
IR090	$N^+ + O_2 \rightarrow NO^+ + O(^1D)$	Viggiano et al. (2003), Fox and Sung (2001), Dotan et al. (1997), O'Keefe et al. (1986)
IR091	$N^+ + O_2 \rightarrow O^+ + NO$	Viggiano et al. (2003), Fox and Sung (2001), Dotan et al. (1997), O'Keefe et al. (1986)
IR092	$N_2^+ + Ar \rightarrow Ar^+ + N_2$	Fox and Sung (2001)
IR093	$N_2^+ + CO \rightarrow N_2 + CO^+$	Anicich (2003)
IR094	$N_2^+ + CO_2 \rightarrow CO_2^+ + N_2$	Fox and Sung (2001)
IR095	$N_2^+ + e^- \rightarrow N + N(^2D)$	Fox and Sung (2001)
IR096	$N_2^+ + e^- \rightarrow N(^2D) + N(^2D)$	Fox and Sung (2001)
IR097	$NO^+ + e^- \rightarrow N(^2D) + O$	Shuman et al. (2015), Fox (2015)
IR098	$NO^+ + e^- \rightarrow N + O$	Shuman et al. (2015), Fox (2015)
IR099	$N_2^+ + N \rightarrow N^+ + N_2$	Ferguson (1973), upper limit
IR100	$N_2^+ + NO \rightarrow N_2 + NO^+$	Scott et al. (1999)
IR101	$N_2^+ + O \rightarrow NO^+ + N(^2D)$	Fox and Sung (2001)
IR102	$N_2^+ + O \rightarrow O^+ + N_2$	Fox and Sung (2001)
IR103	$N_2^+ + O_2 \rightarrow N_2 + O_2^+$	Scott et al. (1999), Fox and Sung (2001)
IR104	$O^+ + C \rightarrow C^+ + O$	Fox and Sung (2001), estimate
IR105	$O^+ + CO_2 \rightarrow O_2^+ + CO$	Anicich (2003)
IR106	$O^+ + e^- \rightarrow O$	McElroy et al. (2013), Nahar (1999), calculated
IR107	$O^+ + H \rightarrow H^+ + O$	McElroy et al. (2013), Stancil et al. (1999)
IR108	$O^+ + N(^2D) \rightarrow N^+ + O$	Bates (1989), Constantinides et al. (1979)
IR109	$O^+ + N_2 \rightarrow NO^+ + N$	Fox and Sung (2001)
IR110	$O^+ + NO \rightarrow NO^+ + O$	Fox and Sung (2001)
IR111	$O^+ + O_2 \rightarrow O + O_2^+$	Fox and Sung (2001)
IR112	$O_2^+ + C \rightarrow CO^+ + O$	Prasad and Huntress Jr (1980) estimate

(continued on next page)

Table C1 (continued)

Number	Reaction	Source
IR113	$O_2^+ + C \rightarrow C^+ + O_2$	Prasad and Huntress Jr (1980) estimate
IR114	$O_2^+ + e^- \rightarrow O + O$	Fox (2012)
IR115	$O_2^+ + e^- \rightarrow O + O(^1D)$	Fox (2012)
IR116	$O_2^+ + e^- \rightarrow O(^1D) + O(^1D)$	Fox (2012)
IR117	$O_2^+ + N \rightarrow NO^+ + O$	Scott et al. (1998)
IR118	$O_2^+ + N(^2D) \rightarrow NO^+ + O$	Fox and Sung (2001)
IR119	$O_2^+ + N(^2D) \rightarrow N^+ + O_2$	Fox and Sung (2001), estimate
IR120	$O_2^+ + NO \rightarrow NO^+ + O_2$	Midey and Viggiano (1999)
IR121	$O_2^+ + N_2 \rightarrow NO^+ + NO$	Ferguson (1973), upper limit
IR122	$N(^2D) + e^- \rightarrow N + e^-$	Berrington and Burke (1981)
IR123	$N(^2D) + NO \rightarrow N_2 + O$	Fell et al. (1990)
IR124	$N(^2D) + O_2 \rightarrow NO + O(^1D)$	Herron (1999)
IR125	$O(^1D) + Ar \rightarrow O + Ar$	Blitz et al. (2004)
IR126	$O(^1D) + CO \rightarrow O + CO$	Schofield (1978)
IR127	$O(^1D) + CO_2 \rightarrow O + CO_2$	Burkholder et al. (2015)
IR128	$O(^1D) + e^- \rightarrow O + e^-$	Berrington and Burke (1981)
IR129	$O(^1D) + H \rightarrow O + H$	Fox (2012)
IR130	$O(^1D) + H_2 \rightarrow OH + H$	Fox (2012)
IR131	$O(^1D) + N_2 \rightarrow O + N_2$	Burkholder et al. (2015)
IR132	$O(^1D) + O \rightarrow O + O$	Fox (2012)
IR133	$O(^1D) + O_2 \rightarrow O + O_2$	Fox (2012)
IR134	$O(^1D) \rightarrow O$	Fox (2012)
IS001	$CO_2 + e^- \rightarrow CO_2^+ + e^- + e^-$	
IS002	$CO + e^- \rightarrow CO^+ + e^- + e^-$	
IS003	$N_2 + e^- \rightarrow N_2^+ + e^- + e^-$	
IS004	$N + e^- \rightarrow N^+ + e^- + e^-$	
IS005	$O_2 + e^- \rightarrow O_2^+ + e^- + e^-$	
IS006	$O + e^- \rightarrow O^+ + e^- + e^-$	

Appendix D. Testing the Mm detection method for baseline and solar flare conditions

The applicability of the Mm detection method is tested for baseline and solar flare conditions. This includes the identification of the solar radiation responsible for the Mm formation in the IonA-2 model, the comparison of the detected Mm parameters with model electron density originating from solar radiation < 1 nm and < 2 nm, investigating the potential occurrence of peaks in the IonA-2 Mm region during solar flares and testing a new parameter for the Mm shape identification.

The part of the solar spectrum responsible for the formation of the detected Mm region is investigated by running the IonA-2 model for the environmental conditions of the MaRS DoY 336 (2005) observation (MCD V5.2 scenario for $L_s = 333.7^\circ$, $lon = 72.7^\circ$, $lat = 66.8^\circ$). Baseline solar flux conditions (φ_b) for DoY 336 (2005) and solar flare (φ_M, φ_X) scenarios are applied to investigate the effect of the varying short wavelength fluxes on the Mm formation and detection. The basic solar radiation data for the IonA-2 model are derived from a combination of the SIP V2.38 (> 10 nm, 1 spectrum/24 h) and the FISM flare V2.0 (≤ 10 nm, 1 spectrum/60s, 0.1 nm resolution) models for Earth. The Mars calibration procedure for solar radiation > 10 nm is described in Peter et al. (2014) and the derived IonA-2 input fluxes at the top of the Mars atmosphere ($\varphi_{\geq 10nm}^*$, with $*$ = b, M or X) are held constant for all three scenarios. The derivation of the input solar radiation ≤ 10 nm differs for the [b] and the [M]/[X] flare scenarios. The FISM solar radiation used in the baseline scenario is extracted at a fixed time (DoY 336 (2005), 1A - 8A integrated flux $\sim 3.7 \cdot 10^{-6} \text{ W m}^{-2}$ at 2:24 h¹) and calibrated to the Mars distance ($\varphi_b^{\leq 10nm}$). For the [M] and [X] scenarios individual flare events are selected from which 1.5 h time sequences of FISM solar spectra with 60s resolution are extracted. In the [M] flare scenario data from 09. June 2007 between 13:30 and 15:00 h with a maximum 1A - 8A integrated flux of $\sim 1.8 \cdot 10^{-5} \text{ W m}^{-2}$ at 13:41 h are applied. The [X] scenario uses data from 09. Sept. 2005 between 2:09 and 3:39 with a maximum integrated flux of $\sim 2 \cdot 10^{-4} \text{ W m}^{-2}$ at 2:59 h. The individual FISM spectra are spatially calibrated to the top of the Mars atmosphere ($\varphi_{\geq 10nm}^{TA, \leq 10nm}$, $*$ = M, X) with the Sun-Mars distance of DoY 336 (2005) and shifted by the difference between the pre-flare baseline flux ($\varphi_{\geq 10nm}^{TA, \leq 10nm}(1)$) and the background scenario flux ($\varphi_b^{\leq 10nm}$): $\varphi_{\geq 10nm}^* = \varphi_{\geq 10nm}^{TA, \leq 10nm} - [\varphi_{\geq 10nm}^{TA, \leq 10nm}(1) - \varphi_b^{\leq 10nm}]$ to avoid large discontinuities in the solar flux model input. Convergent IonA-2 runs for the full solar radiation range φ_* , radiation larger 1 nm ($\varphi_{\geq 1nm}^*$) and larger 2 nm ($\varphi_{\geq 2nm}^*$) provide the associated model electron densities $n_{e,*}$, $n_{e,*}^{\geq 1nm}$ and $n_{e,*}^{\geq 2nm}$. Mm parameters are determined from the detected Mm region Δ_{*}^{det} , the residual electron densities originating from 1 nm solar radiation ($\Delta_{*}^{1nm} = n_{e,*} - n_{e,*}^{\geq 1nm}$), and 2 nm radiation ($\Delta_{*}^{2nm} = n_{e,*} - n_{e,*}^{\geq 2nm}$).

Fig. D1 illustrates the relation between the individual Mm parameters derived from the baseline scenario. While the Mm altitude ranges derived

¹ M to C class flares have been observed at DoY 336 (2005) close to 2:24 h, but no designated flare is available at that time in the National Oceanic and Atmospheric Administration (NOAA) solar flare list (www.ngdc.noaa.gov/stp/space-weather/solar-data/solar-features/solar-flares/).

from Δ_b^{det} and Δ_b^{1nm} both cover the lowest region of the electron density profile only, Δ_b^{2nm} also affects the M1 peak region (Fig. D1a,b). The diurnal variation of the solar radiation is in general reflected by the derived Mm parameters. The Mm are, however, not symmetric to 12 h MLST due to changes in the underlying neutral atmosphere. The Δ_b^{det} Mm TEC (Fig. D1c), peak electron density (Fig. D1d) and altitude (Fig. D1e) are usually found within the boundaries of the Δ_b^{1nm} and Δ_b^{2nm} Mm parameters and follow their overall trend. It can therefore be concluded that the applied Mm detection method provides Mm parameters originating from the solar radiation below 2 nm for the solar conditions of the baseline scenario. The slope of the lower visible Mm region α_{Mm} is used as Mm shape indicator. $\alpha_{Mm}(\Delta_b^{det})$ and $\alpha_{Mm}(\Delta_b^{1nm})$ are determined from a straight line fit on the Mm altitude range between $3\sigma_{nse}$ and the Mm peak altitude - 0.5 km. $\alpha_{Mm}(\Delta_b^{2nm})$ is determined between $3\sigma_{nse}$ and the Mm peak altitude - 5 km due to its more elongated shape.

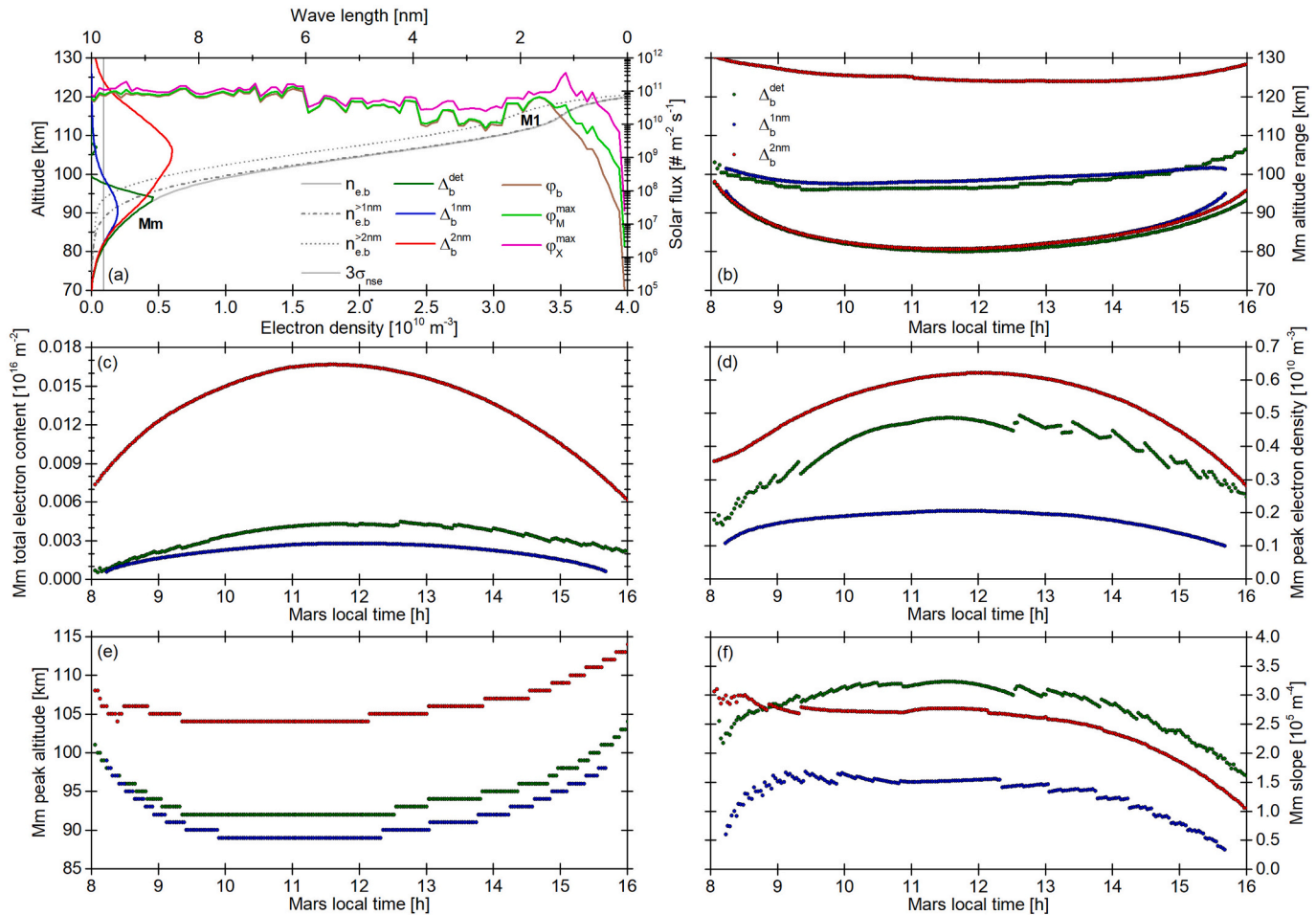


Fig. D1. Dayside IonA-2 Mm parameters for the MaRS DoY 336 (2005) observation conditions and the baseline φ_b solar flux scenario. The assumed noise level σ_{nse} for the Mm parameter calculations is $3 \cdot 10^8 \text{ m}^{-3}$. (a) IonA-2 model electron densities and associated Δ_b^{det} , Δ_b^{1nm} and Δ_b^{2nm} for 13h MLST. φ_b , φ_M^{max} and φ_X^{max} are the solar flux spectra at the top of the Mars atmosphere for the baseline scenario and at the times where the φ_M and φ_X radiation < 2 nm reach their respective maxima. (b) – (f) Mm parameters derived from Δ_b^{det} , Δ_b^{1nm} and Δ_b^{2nm} .

No slope is calculated if the altitude difference between the lower model boundary (65 km altitude) and $3\sigma_{nse}$ is lower than 3 km to avoid model boundary effects. δ_{Mm} is the maximum difference between the fitted line and the model electron density in the designated fitting area. It is found that $\delta_{Mm} < 3\sigma_{nse}$ for all baseline scenario results. A straight line is therefore an appropriate Mm shape indicator for the undisturbed solar conditions of the baseline scenario. Fig. D1f illustrates the slopes derived from the detected and residual Mm for the baseline scenario. $\alpha_{Mm}(\Delta_b^{det})$ follows the diurnal trend of $\alpha_{Mm}(\Delta_b^{1nm})$, but is in general slightly larger than $\alpha_{Mm}(\Delta_b^{2nm})$. The reason for that is the small amount of electron density in Δ_b^{det} caused by solar radiation larger than 2 nm.

Fig. D2 illustrates the effect of the 1.5 h φ_M flare spectra sequence on the dayside ionosphere of Mars. φ_M is applied at each Mars hour between 8 and 15 h MLST, while the IonA-2 model provides the associated ionospheric response in 2 min intervals for each computed flare event. The comparison of the [M] flare results with the baseline scenario in Fig. D2a indicates that the flux enhancement in the wavelength range < 2 nm leads to a decrease of the ionospheric base and to an enhancement of the Mm and M1 regions. While the Mm lower boundary is decreasing for Δ_M^{det} , Δ_M^{1nm} and Δ_M^{2nm} , only Δ_M^{1nm} shows a significant increase of the upper Mm altitude boundary (Fig. D2b). The enhancement of the Mm region is reflected in increased Mm TEC and

peak electron density parameters (Fig. D2c,d) in correlation with the energy increase in the shorter wavelengths. The Δ_M^{det} Mm parameters follow the overall trend of Δ_M^{1nm} and Δ_M^{2nm} and are in general found within their parameter boundaries. The detected Mm parameters therefore still represent the electron density originating from the solar radiation < 2 nm, similar to the baseline scenario. $\alpha_{Mm}(\Delta_M^{det})$, $\alpha_{Mm}(\Delta_M^{1nm})$ and $\alpha_{Mm}(\Delta_M^{2nm})$ increase for increasing ϕ_M^{1nm} and ϕ_M^{2nm} . δ_{Mm} is smaller than $3\sigma_{nse}$ for Δ_M^{det} , Δ_M^{1nm} and Δ_M^{2nm} , indicating that a straight line is still a good approximation for the model Mm shape for flare sizes similar to those in the [M] scenario.

Fig. D3 illustrates the effect of the ϕ_X flare spectra sequence on the Mars dayside ionosphere. The strong increase in solar radiation at the peak of the flare causes a strong altitude decrease of the ionospheric base. No peak structures in the Mm region are, however, seen in the IonA-2 model output for any applied ϕ_X solar spectrum. The detected Mm parameters highly underestimate the effect of the electron density originating from the solar radiation < 1 and < 2 nm. The Mm slopes $\alpha_{Mm}(\Delta_M^{det})$, $\alpha_{Mm}(\Delta_M^{1nm})$ and $\alpha_{Mm}(\Delta_M^{2nm})$ are, however, still in good agreement, except for the region around $\phi_{X,max}^{1nm}$ and $\phi_{X,max}^{2nm}$, where $\alpha_{Mm}(\Delta_M^{det})$ is slightly underestimated or not available. δ_{Mm} is still small ($< 3\sigma_{nse}$), except for few data points close to the peak of the flare. This makes $\alpha_{Mm}(\Delta_M^{det})$ a good proxy for the shape of the observed Mm.

The Mm detection method reliably provides IonA-2 Mm parameters caused by the electron density originating from solar radiation < 2 nm for baseline solar radiation conditions and smaller [M] flares. Larger flares cause a strong decrease of the whole ionospheric base, which makes the Mm detection method not applicable. The Mm slope provides a good base for shape determination up to the solar radiation range of smaller [X] flares. Larger flares produce non-neglectable amounts of electron density at 65 km altitude. A lower model boundary is needed for their investigation to avoid boundary condition effects on the model results. None of the applied flare spectra resulted in detectable peaks in the Mm region.

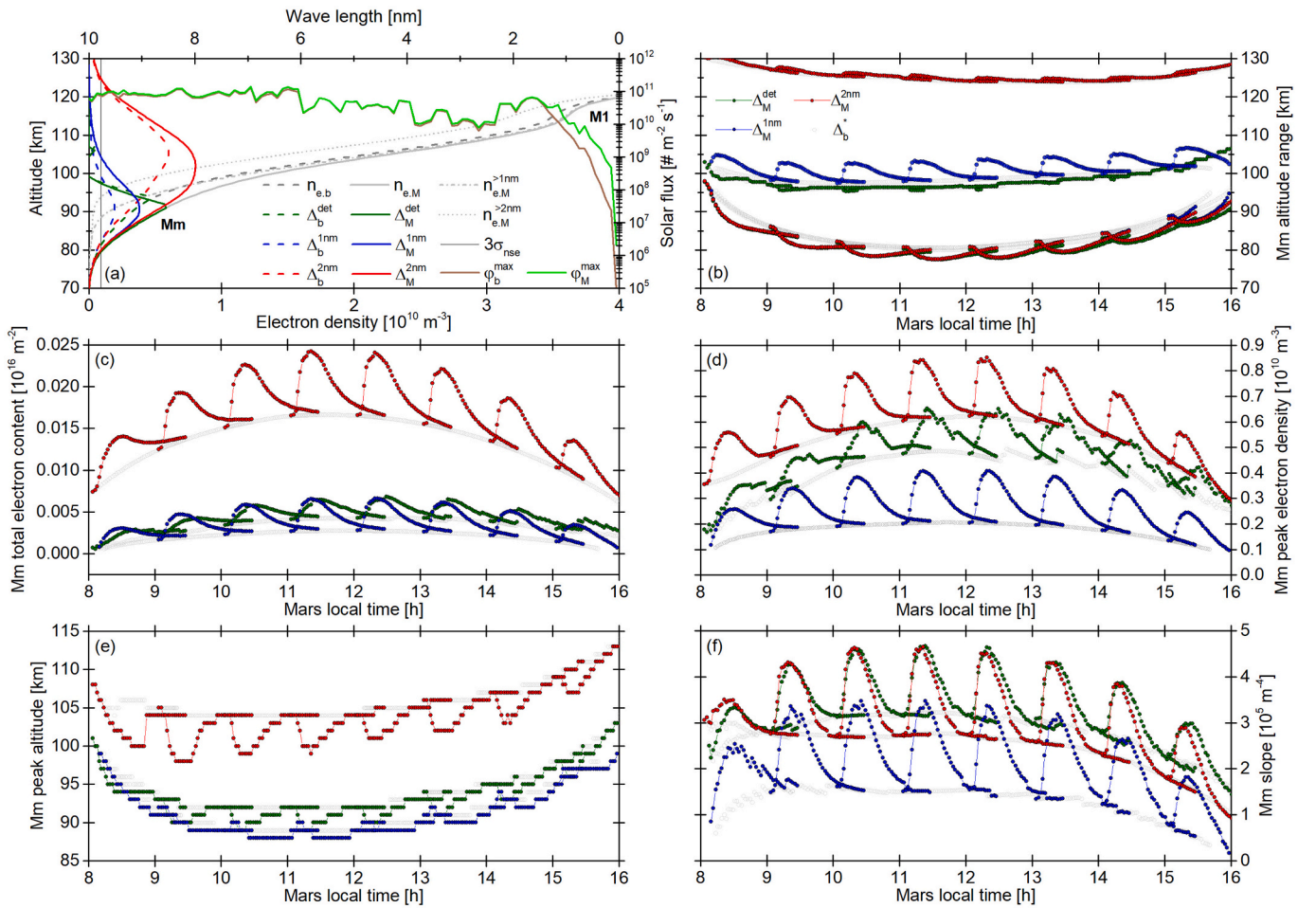


Fig. D2. [M] flare scenario for DoY 336 (2005) conditions compared with the [b] scenario. (a) Model electron densities and associated Δ_M^{det} , Δ_M^{1nm} and Δ_M^{2nm} at ϕ_M^{max} of the 13h MLST IonA-2 model run. (b) – (f) Mm parameters derived from Δ_M^{det} , Δ_M^{1nm} and Δ_M^{2nm} . Gray markings indicate the [b] scenario results from Fig. D1.

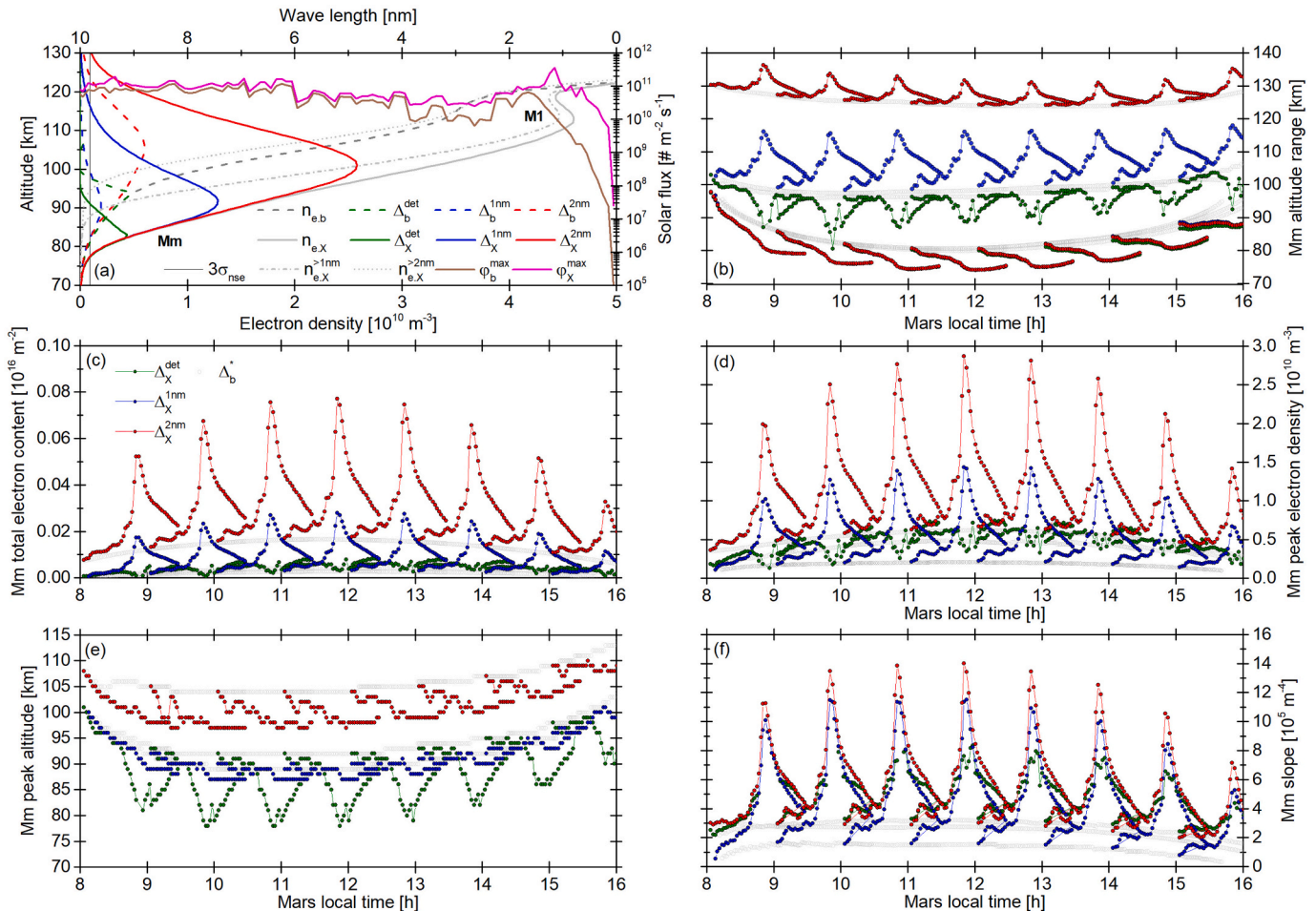


Fig. D3. [X] flare scenario for DoY 336 (2005) conditions compared with the [b] baseline scenario. (a) Model electron densities and associated ΔX_X^{det} , ΔX_X^{1nm} and ΔX_X^{2nm} at φ_X^{max} in the 13h MLST IonA-2 model run. (b) – (f) Mm parameters derived from ΔX_X^{det} , ΔX_X^{1nm} and ΔX_X^{2nm} . Gray markings indicate the [b] scenario results from Fig. D1.

References

- Albee, A.L., Palluconi, F.D., Arvidson, R.E., 1998. Mars global surveyor mission: overview and status. *Science* 279 (5357), 1671–1672.
- Anicich, Vincent G., 2003. An Index of the Literature for Biomolecular Gas Phase Cation-Molecule Reaction Kinetics. JPL (JPL-Publ-03-19).
- Aschwanden, Markus J., 1994. Irradiance observations of the 1–8 Å solar soft X-ray flux from GOES. *Sol. Phys.* 152 (1), 53–59. <https://doi.org/10.1007/BF01473183>.
- Atkinson, R., Baulch, D.L., Cox, R.A., Hampson, R.F., Kerr, J.A., Troe, J., 1989. Evaluated kinetic and photochemical data for atmospheric chemistry. Supplement III. IUPAC subcommittee on gas kinetic data evaluation for atmospheric chemistry. *J. Phys. Chem. Ref. Data* 18 (2), 881–1097. <https://doi.org/10.1063/1.555832>.
- Banks, Peter Morgan, Kockarts, Gaston, 1973. *Aeronomy – Part A*. Acad. Press, New York, NY.
- Bates, David R., 1989. Theoretical considerations regarding some inelastic atomic collision processes of interest in aeronomy. Deactivation and charge transfer. *Planet. Space Sci.* 37 (3), 363–368. [https://doi.org/10.1016/0032-0633\(89\)90033-0](https://doi.org/10.1016/0032-0633(89)90033-0).
- Berrington, K.A., Burke, P.G., 1981. Effective collision strengths for forbidden transitions in e-N and e-o scattering. *Planet. Space Sci.* 29 (3), 377–381. [https://doi.org/10.1016/0032-0633\(81\)90026-X](https://doi.org/10.1016/0032-0633(81)90026-X).
- Bertaux, Jean-Loup, Leblanc, François, Perrier, Séverine, Quémenerais, E., Korablev, Oleg, Dimarellis, E., et al., 2005. Nightglow in the upper atmosphere of Mars and implications for atmospheric transport. *Science* (New York, N.Y.) 307 (5709). <https://doi.org/10.1126/science.11106957>. S. 566–569.
- Blitz, Mark A., Dillon, Terry J., Heard, Dwayne E., Pilling, Michael J., Trought, Ian D., 2004. Laser induced fluorescence studies of the reactions of $O(^1D_2)$ with N_2 , O_2 , N_2O , CH_4 , H_2 , CO_2 , Ar, Kr and $n-C_4H_{10}$. *Phys. Chem. Chem. Phys.* 6 (9) <https://doi.org/10.1039/b400283k>. S. 2162.
- Borodi, G., Luca, A., Gerlich, D., 2009. Reactions of CO_2^+ with H, H_2 and deuterated analogues. *Int. J. Mass Spectrom.* 280 (1–3), 218–225. <https://doi.org/10.1016/j.ijms.2008.09.004>.
- Bougher, Stephen Wesley, Engel, Steffi, Hinson, David P., Murphy, J.R., 2004. MGS Radio Science electron density profiles: interannual variability and implications for the Martian neutral atmosphere. *J. Geophys. Res.* 109 (E3) <https://doi.org/10.1029/2003JE002154>.
- Brune, W.H., Schwab, James J., Anderson, J.G., 1983. Laser magnetic resonance, resonance fluorescence, resonance absorption studies of the reaction kinetics of atomic oxygen + hydroxyl.fwdarw. atomic hydrogen + molecular oxygen, atomic oxygen + perhydroxyl.fwdarw. hydroxyl + molecular oxygen, atomic nitrogen + hydroxyl.fwdarw. atomic hydrogen + nitric oxide, atomic nitrogen + perhydroxyl.fwdarw. products at 300 K between 1 and 5 torr. *J. Phys. Chem.* 87 (22) <https://doi.org/10.1021/j100245a034>. S. 4503–4514.
- Burkholder, J.B., Sander, S.P., Abbatt, J., Barker, J.R., Huie, R.E., Kolb, C.E., et al., 2015. *Chemical Kinetics and Photochemical Data for Use in Atmospheric Studies, Evaluation Number 18*. Hg. v. JPL Publication 15-10, Jet Propulsion Laboratory, Pasadena.
- Chamberlin, P.C., Woods, T.N., Eparvier, F.G., 2007. Flare Irradiance Spectral Model (FISM): daily component algorithm and results. *Space Weather* 5, S07005. <https://doi.org/10.1029/2007SW000316>.
- Chapman, S., Cowling, T.G., 1939. *The Mathematical Theory of Nonuniform Gases*. Cambridge Univ. Pr, New York.
- Chastaing, Delphine, Picard, Le, Sébastien, D., Sims, Ian R., 2000. Direct kinetic measurements on reactions of atomic carbon, $C(^3P)$, with O_2 and NO at temperatures down to 15 K. *J. Chem. Phys.* 112 (19), 8466–8469. <https://doi.org/10.1063/1.481448>.
- Colegrove, F.D., Johnson, F.S., Hanson, W.B., 1966. Atmospheric composition in the lower thermosphere. *J. Geophys. Res.* 71 (9), 2227–2236. <https://doi.org/10.1029/JZ071i009p02227>.
- Constantinides, E.R., Black, J.H., Dalgarno, A., Hoffman, J.H., 1979. The photochemistry of N^+ ions. *Geophys. Res. Lett.* 6 (7), 569–572. <https://doi.org/10.1029/GL006i007p00569>.
- Creasey, John E., Forbes, Jeffrey M., Keating, Gerald M., 2006. Density variability at scales typical of gravity waves observed in Mars' thermosphere by the MGS accelerometer. *Geophys. Res. Lett.* 33 (22).

- Crismani, M.M.J., Schneider, Nicholas M., Plane, John M.C., Evans, J.S., Jain, S.K., Chaffin, M.S., et al., 2017. Detection of a persistent meteoric metal layer in the Martian atmosphere. *Nat. Geosci.* 10, S. 401–404.
- Crismani, M.M.J., Deighan, J., Schneider, N.M., Plane, J.M.C., Withers, P., Halekas, J., et al., 2019. Localized ionization hypothesis for transient ionospheric layers. *J. Geophys. Res.* <https://doi.org/10.1029/2018JA026251>.
- Dotan, I., Hiel, Peter M., Morris, Robert A., Viggiano, A.A., 1997. Rate constants for the reactions of N^+ and N_2^+ with O_2 as a function of temperature (300–1800 K). *Int. J. Mass Spectrom. Ion Process.* 167–168, 223–230. [https://doi.org/10.1016/S0168-1176\(97\)00077-3](https://doi.org/10.1016/S0168-1176(97)00077-3).
- Dotan, Itzhak, Midey, Anthony J., Viggiano, A.A., 1999. Rate constants for the reactions of Ar^+ with CO_2 and SO_2 as a function of temperature (300–1500 K). *J. Am. Soc. Mass Spectrom.* 10 (9), 815–820. [https://doi.org/10.1016/S1044-0305\(99\)00056-2](https://doi.org/10.1016/S1044-0305(99)00056-2).
- Du, M.L., Dalgarno, A., 1990. The radiative association of N and O atoms. *J. Geophys. Res.* 95 (A8) <https://doi.org/10.1029/JA095A08p12265>. S. 12265.
- England, Scott L., Liu, Guiping, Yigit, Erdal, Mahaffy, Paul R., Elrod, M., Benna, Mehdi, et al., 2017. MAVEN NGIMS observations of atmospheric gravity waves in the Martian thermosphere. *J. Geophys. Res. Space Physics* 122 (2). S. 2310–2335.
- Fahey, D.W., Fehsenfeld, F.C., Ferguson, Eldon E., 1981. Rate constant for the reaction $C^+ + CO_2$ at collision energies 0.04 to 2.5 eV. *Geophys. Res. Lett.* 8 (10), 1115–1117. <https://doi.org/10.1029/GL008i010p01115>.
- Fehsenfeld, F.C., Ferguson, Eldon E., 1972. Recent laboratory measurements of D- and E-region ion-neutral reactions. *Radio Sci.* 7 (1), 113–115. <https://doi.org/10.1029/RS007i001p00113>.
- Fehsenfeld, F.C., Dunkin, D.B., Ferguson, Eldon E., 1970. Rate constants for the reaction of CO_2^+ with O_2 and NO ; N_2^+ with O and NO ; and O_2^+ with NO . *Planet. Space Sci.* 18 (8), 1267–1269. [https://doi.org/10.1016/0032-0633\(70\)90216-3](https://doi.org/10.1016/0032-0633(70)90216-3).
- Fell, C., Steinfeld, J.I., Miller, S., 1990. Quenching of $N(^2D)$ by $O(^3P)$. *J. Chem. Phys.* 92 (8), 4768–4777. <https://doi.org/10.1063/1.457694>.
- Ferguson, Eldon E., 1973. Rate constants of thermal energy binary ion-molecule reactions of aeronomic interest. *At. Data Nucl. Data Tables* 12 (2), 159–178. [https://doi.org/10.1016/0092-640X\(73\)90017-X](https://doi.org/10.1016/0092-640X(73)90017-X).
- Fernandez, Abel, Goumri, A., Fontijn, Arthur, 1998. Kinetics of the reactions of $N(^4S)$ atoms with O_2 and CO_2 over wide temperature ranges. *J. Phys. Chem. A* 102 (1), 168–172. <https://doi.org/10.1021/jp972365k>.
- Fjeldbo, G., Eshleman, V.R., 1965. The bistatic radar-occultation method for the study of planetary atmospheres. *J. Geophys. Res.* 70 (13), 3217–3225. <https://doi.org/10.1029/JZ070i013p03217>.
- Fjeldbo, Gunnar, Kliore, Arvydas J., von Eshleman, R., 1971. The neutral atmosphere of Venus as studied with the mariner V radio occultation experiments. *Astron. J.* 76, 123–140. <https://doi.org/10.1086/111096>.
- Fletcher, Karen (Hg.), 2009. *Mars Express. The scientific investigations*. ESA Communication Production Office, Noordwijk, the Netherlands.
- Fox, Jane L., 2004. Response of the Martian thermosphere/ionosphere to enhanced fluxes of solar soft X rays. *J. Geophys. Res.* 109 (A11310).
- Fox, Jane L., 2009. Morphology of the dayside ionosphere of Mars: implications for ion outflows. *J. Geophys. Res. Planets* 114, E12005. <https://doi.org/10.1029/2009JE003432>.
- Fox, Jane L., 2012. The ionospheric source of the red and green lines of atomic oxygen in the Venus nightglow. *Icarus* 221 (2), S. 787–799. <https://doi.org/10.1016/j.icarus.2012.09.007>.
- Fox, Jane L., 2015. The chemistry of protonated species in the martian ionosphere. *Icarus* 252, S. 366–392. <https://doi.org/10.1016/j.icarus.2015.01.010>.
- Fox, Jane L., Sung, K.Y., 2001. Solar activity variations of the Venus thermosphere/ionosphere. *J. Geophys. Res.* 106 (A10), 21305–21335. <https://doi.org/10.1029/2001JA000069>.
- Fox, Jane L., Zhou, P., Bougher, Stephen Wesley, 1996. The Martian thermosphere/ionosphere at high and low solar activities. *Adv. Space Res.* 17 (11).
- Fritts, David C., Wang, Ling, Tolson, Robert H., 2006. Mean and gravity wave structures and variability in the Mars upper atmosphere inferred from Mars Global Surveyor and Mars Odyssey aerobraking densities. *J. Geophys. Res.* 111.
- Gear, Charles William, 1971. *Numerical Initial Value Problems in Ordinary Differential Equations*. Prentice-Hall, Englewood Cliffs N.J (Prentice-Hall series in automatic computation).
- Geppert, Wolf D., Thomas, Richard, Ehlerding, Anneli, Semaniak, Jacek, Österdahl, Fabian, Uggla, af, Magnus, et al., 2004. Extraordinary branching ratios in astrophysically important dissociative recombination reactions. *Faraday Discuss.* 127 (E12), 425–437. <https://doi.org/10.1039/B314005A>.
- González-Galindo, F., Chaufray, J.-Y., López-Valverde, M.A., Gilli, G., Forget, F., Leblanc, F., et al., 2013. Three-dimensional Martian ionosphere model. I. The photochemical ionosphere below 180 km. *J. Geophys. Res.* 118 (10), S. 2105–2123. <https://doi.org/10.1002/jgre.20150>.
- Gopalswamy, N., 2016. History and development of coronal mass ejections as a key player in solar terrestrial relationship. *Geosci. Lett.* 3 (1) <https://doi.org/10.1186/s40562-016-0039-2>. S. 195.
- Gougousi, Theodosia, Golde, Michael F., Johnsen, Rainer, 1997. Electron-ion recombination rate coefficient measurements in a flowing afterglow plasma. *Chem. Phys. Lett.* 265 (3–5), 399–403. [https://doi.org/10.1016/S0009-2614\(96\)01488-1](https://doi.org/10.1016/S0009-2614(96)01488-1).
- Grebowsky, J.M., Benna, M., Plane, J.M.C., Collinson, G.A., Mahaffy, P.R., Jakosky, B.M., 2017. Unique, non-Earthlike, meteoritic ion behavior in upper atmosphere of Mars. *Geophys. Res. Lett.* 44 (7), 3066–3072. <https://doi.org/10.1002/2017GL072635>.
- Hanson, W.B., Sanatani, S., Zuccaro, D.R., 1977. The Martian ionosphere as observed by the viking retarding potential analyzers. *J. Geophys. Res.* 82 (28), 4351–4363. <https://doi.org/10.1029/JA082i028p04351>.
- Hassler, D.M., Zeitlin, C., Wimmer-Schweingruber, R.F., Böttcher, S., Martin, C., Andrews, J., et al., 2012. The radiation assessment detector (RAD) investigation. *Space Sci. Rev.* 170 (1–4), 503–558. <https://doi.org/10.1007/s11214-012-9913-1>.
- Hathaway, David H., 2015. The solar cycle. *Living Rev. Solar Physics* 12. <https://doi.org/10.1007/lrsp-2015-4>. S. 4.
- Herron, John T., 1999. Evaluated chemical kinetics data for reactions of $N(^2D)$, $N(^2P)$, and $N_2(A^3\Sigma_u^+)$ in the gas phase. *J. Phys. Chem. Ref. Data* 28 (5), 1453–1483. <https://doi.org/10.1063/1.556043>.
- Hinson, David P., Simpson, Richard A., Twicken, Joseph D., Tyler, G. Leonard, 1999. Initial results from radio occultation measurements with Mars Global Surveyor. *J. Geophys. Res.* 104 (E11), 26997–27012.
- Huebner, W.F., Mukherjee, J., 2015. Photoionization and photodissociation rates in solar and blackbody radiation fields. *Planet. Space Sci.* 106, 11–45.
- Hunten, Donald M., 1973. The escape of light gases from planetary atmospheres. *J. Atmos. Sci.* 30 (8), S. 1481–1494. [https://doi.org/10.1175/1520-0469\(1973\)030<1481:TEOLGF>2.0.CO;2](https://doi.org/10.1175/1520-0469(1973)030<1481:TEOLGF>2.0.CO;2).
- Jacobson, Mark Z., 2007. *Fundamentals of Atmospheric Modeling*, 2nd ed. Cambridge University Press, Cambridge. transferred to digital print.
- Jakosky, Bruce M., Grebowsky, Joseph M., Luhmann, Janet G., Brain, David A., 2015a. Initial results from the MAVEN mission to Mars. *Geophys. Res. Lett.* 42 (21), S. 8791–8802. <https://doi.org/10.1002/2015GL065271>.
- Jakosky, Bruce M., Lin, Robert P., Grebowsky, Joseph M., Luhmann, Janet G., Mitchell, D.F., Beutelschies, G., et al., 2015b. The Mars atmosphere and volatile evolution (MAVEN) mission. *Space Sci. Rev.* 195 (1), 3–48. <https://doi.org/10.1007/s11214-015-0139-x>.
- Kliore, Arvydas J., Cain, Dan L., Levy, Gerald S., Eshleman, R. von, Fjeldbo, Gunnar, Drake, Frank D., 1965. Occultation experiment: results of the first direct measurement of Mars's atmosphere and ionosphere. *Science* (New York, N.Y.) 149 (3689). <https://doi.org/10.1126/science.149.3689.1243>. S. 1243–1248.
- Kockarts, G., 2002. Aeronomy, a 20th century emergent science. The role of solar Lyman series. *Ann. Geophys.* 20 (5), 585–598. <https://doi.org/10.5194/angeo-20-585-2002>.
- Krasnopolsky, Vladimir A., 1986. Photochemistry of the Atmospheres of Mars and Venus. Springer, Berlin, Heidelberg. <https://doi.org/10.1007/978-3-642-70401-7> (Physics and Chemistry in Space, 13). Online verfügbar unter.
- Krasnopolsky, Vladimir A., 1993. Photochemistry of the Martian atmosphere (mean conditions). *Icarus* 101, S. 313–332.
- Lefèvre, F., Krasnopolsky, Vladimir A., Zurek (Hg.), R.W., 2017. Atmospheric photochemistry. In: Haberle, R.M., Clancy, R.T., Forget, F., Smith, Michael D. (Eds.), *The Atmosphere and Climate of Mars*. Cambridge Univ. Pr, Cambridge, pp. S. 405–432.
- Lewis, Stephen R., Collins, Matthew, Read, Peter L., Forget, François, Hourdin, Frédéric, Fournier, Richard, et al., 1999. A climate database for Mars. *J. Geophys. Res.* 104 (E10), S. 24177–24194. <https://doi.org/10.1029/1999JE001024>.
- Lillis, Robert J., Brain, David A., England, Scott L., Withers, Paul, Fillingim, Matthew O., Safaieili, Ali, 2010. Total electron content in the Mars ionosphere. Temporal studies and dependence on solar EUV flux. *J. Geophys. Res.* 115 (A11) <https://doi.org/10.1029/2010JA015698>.
- Lollo, Withers P., Fallows, K., Girazian, Z., Matta, M., Chamberlin, P.C., 2012. Numerical simulations of the ionosphere of Mars during a solar flare. *J. Geophys. Res. Space Physics* 117. <https://doi.org/10.1029/2011JA017399>. A05314.
- Mahaffy, Paul R., Benna, Mehdi, Elrod, M., Yelle, Roger V., Bougher, Stephen Wesley, Stone, S.W., Jakosky, Bruce M., 2015a. Structure and composition of the neutral upper atmosphere of Mars from the MAVEN NGIMS investigation. *Geophys. Res. Lett.* 42 (21), 8951–8957. <https://doi.org/10.1002/2015GL065329>.
- Mahaffy, Paul R., Benna, Mehdi, King, Todd, Harpold, Daniel N., Arvey, Robert, Barciniak, Michael, et al., 2015b. The neutral gas and ion mass spectrometer on the Mars atmosphere and volatile evolution mission. *Space Sci. Rev.* 195 (1), 49–73. <https://doi.org/10.1007/s11214-014-0091-1>.
- Mahajan, K.K., Lodhi, Neelish K., Singh, Sachchidanand, 2009. Ionospheric effects of solar flares at Mars. *Geophys. Res. Lett.* 36 (15) <https://doi.org/10.1029/2009GL039454>.
- Mathews, J.D., 1998. Sporadic E: current views and recent progress. *J. Atmos. Sol. Terr. Phys.* 60 (4), 413–435.
- Matta, M., Withers, P., Mendillo, M., 2013. The composition of Mars' topside ionosphere: effects of hydrogen. *JGR Space Phys.* 118, 2681–2693. <https://doi.org/10.1002/jgra.50104>.
- McClintock, William E., Schneider, Nicholas M., Holsclaw, Gregory M., Clarke, John T., Hoskins, Alan C., Stewart, Ian, et al., 2015. The imaging ultraviolet spectrograph (IUVS) for the MAVEN mission. *Space Sci. Rev.* 195 (1), 75–124. <https://doi.org/10.1007/s11214-014-0098-7>.
- McElroy, D., Walsh, C., Markwick, A.J., Cordiner, M.A., Smith, K., Millar, T.J., 2013. The UMIST database for astrochemistry 2012. *Astron. Astrophys.* 550 <https://doi.org/10.1051/0004-6361/201220465>. A36.
- Mendillo, Michael, Withers, Paul, Hinson, David P., Rishbeth, Henry, Reinisch, Bodo, 2006. Effects of solar flares on the ionosphere of Mars. *Science* 311 (5764), S. 1135–1138. <https://doi.org/10.1126/science.1122099>.
- Midey, Anthony J., Viggiano, A.A., 1999. Rate constants for the reaction of O_2^+ with NO from 300 to 1400 K. *J. Chem. Phys.* 110 (22), S. 10746–10748. <https://doi.org/10.1063/1.479017>.
- Millour, E., Forget, François, Spiga, A., Navarro, T., Madeleine, J.-B., Montabone, L., et al., 2015. The Mars Climate Database (MCD version 5.2). Paper presented at the EPSC 2015 in Nantes. European Planetary Science Congress 2015. Nantes, 2015.
- Molina-Cuberos, Gregorio J., Witasse, Olivier, Lebreton, Jean-Pierre, Rodrigo, Rafael, López-Moreno, José J., 2003. Meteoric ions in the atmosphere of Mars. *Planet. Space Sci.* 51 (3), 239–249. [https://doi.org/10.1016/S0032-0633\(02\)00197-6](https://doi.org/10.1016/S0032-0633(02)00197-6).

- Molina-Cuberos, Gregorio J., López-Moreno, José J., Arnold, F., 2008. Meteoric layers in planetary atmospheres. *Space Sci. Rev.* 137 (1–4), 175–191. <https://doi.org/10.1007/s11214-008-9340-5>.
- Morgan, D.D., Gurnett, D.A., Kirchner, D.L., Huff, R.L., Brain, David A., Boynton, W.V., et al., 2006. Solar control of radar wave absorption by the Martian ionosphere. *Geophys. Res. Lett.* 33 (13) <https://doi.org/10.1029/2006GL026637>. S. 495.
- Morschhauser, A., Lesur, V., Grott, M., 2014. A spherical harmonic model of the lithospheric magnetic field of Mars. *J. Geophys. Res.* 119 (6), 1162–1188. <https://doi.org/10.1002/2013JE004555>.
- Nahar, Sultana N., 1999. Electron-ion recombination rate coefficients, photoionization cross sections, and ionization fractions for astrophysically abundant elements. II. Oxygen Ions. *Astrophys. J. Suppl. Ser.* 120 (1), 131–145. <https://doi.org/10.1086/313173>.
- Neufeld, Philip D., Janzen, A.R., Aziz, R.A., 1972. Empirical equations to calculate 16 of the transport collision integrals $\Omega(l,s)^*$ for the Lennard-Jones (12–6) potential. *J. Chem. Phys.* 57 (3), 1100–1102. <https://doi.org/10.1063/1.1678363>.
- O’Keefe, A., Mauclair, G., Parent, D., Bowers, M.T., 1986. Product energy disposal in the reaction of $N^+(^3P)$ with $O_2(^3\Sigma^-)$. *J. Chem. Phys.* 84 (1), 215–219. <https://doi.org/10.1063/1.450173>.
- Pandya, B.M., Haider, S.A., 2014. Numerical simulation of the effects of meteoroid ablation and solar EUV/X-ray radiation in the dayside ionosphere of Mars: MGS/MEX observations. *J. Geophys. Res. Space Physics* 119 (11), 9228–9245.
- Pätzold, Martin, Neubauer, F.M., Carone, Ludmila, Hagermann, A., Stanzel, Christina, Häusler, Bernd, et al., 2004. MaRS: Mars express orbiter radio science. In: Wilson (Hg.), Andrew (Ed.), Mars Express. The Scientific Payload. ESA Publications Division, Noordwijk (1240), S. 140–163.
- Pätzold, Martin, Tellmann, Silvia, Häusler, Bernd, Hinson, David P., Schaa, Ralf, Tyler, G. Leonard, 2005. A sporadic high layer in the ionosphere of Mars. *Science* 310, 837–839.
- Pätzold, Martin, Tellmann, Silvia, Andert, T., Carone, Ludmila, Fels, M., Schaa, Ralf, et al., 2009. MaRS: Mars express radio science experiment. In: Fletcher (Hg.), Karen (Ed.), Mars Express. The scientific Investigations. ESA Communication Production Office, Noordwijk, the Netherlands. S. 217–245.
- Pätzold, Martin, Häusler, Bernd, Tyler, G. Leonard, Andert, T., Asmar, Sami W., Bird, Michael K., et al., 2016. Mars express 10 years at Mars. Observations by the Mars express radio science experiment (MaRS). *Planet. Space Sci.* 127, 44–90. <https://doi.org/10.1016/j.pss.2016.02.013>.
- Pesnell, William Dean, Grebowsky, Joseph M., 2000. Meteoric magnesium ions in the Martian atmosphere. *J. Geophys. Res.* 105 (E1), 1695–1707.
- Peter, Kerstin, 2018. Small Scale Disturbances in the Lower Dayside Ionosphere of Mars as Seen by the Radio Science Experiment MaRS on Mars Express. PhD thesis. Universität zu Köln, Köln. Rheinisches Institut für Umweltforschung. <http://kups.uni-koeln.de/id/eprint/8110>.
- Peter, Kerstin, Pätzold, Martin, Molina-Cuberos, Gregorio J., Witasse, Olivier, González-Galindo, Francisco, Withers, Paul, et al., 2014. The dayside ionospheres of Mars and Venus. Comparing a one-dimensional photochemical model with MaRS (Mars Express) and VeRa (Venus Express) observations. *Icarus* 233, 66–82. <https://doi.org/10.1016/j.icarus.2014.01.028>.
- Poling, Bruce E., Prausnitz, John M., O’Connell, John, 2001. *The Properties of Gases and Liquids*, 5. ed. McGraw-Hill, New York NY u.a.
- Prasad, S.S., Huntress Jr., W.T., 1980. A model for gas phase chemistry in interstellar clouds. I - The basic model, library of chemical reactions, and chemistry among C, N, and O compounds. *Astrophys. J. Suppl. Ser.* 43 <https://doi.org/10.1086/190665>. S. 1.
- Reames, Donald V., 1999. Particle acceleration at the Sun and in the heliosphere. *Space Sci. Rev.* 90 (3/4), 413–491. <https://doi.org/10.1023/A:1005105831781>.
- Rishbeth, Henry, Mendillo, Michael, 2004. Ionospheric layers of Mars and Earth. *Planet. Space Sci.* 52 (9), 849–852. <https://doi.org/10.1016/j.pss.2004.02.007>.
- Rohrbaugh, R.P., Nisbet, J.S., Bleuler, E., Herman, J.R., 1979. The effect of energetically produced O_2^+ on the ion temperatures of the Martian thermosphere. *J. Geophys. Res.* 84 (A7), 3327–3338. <https://doi.org/10.1029/JA084iA07p03327>.
- Sánchez-Cano, Beatriz, Lester, Mark, Witasse, Olivier, Blelly, Pierre-Louis, Indurain, Mikel, Cartacci, Marco, et al., 2018. Spatial, seasonal, and solar cycle variations of the Martian Total Electron Content (TEC). Is the TEC a good tracer for atmospheric cycles? *J. Geophys. Res.* 123 (7), 1746–1759. <https://doi.org/10.1029/2018JE005626>.
- Sander, S.P., Abbatt, J.R., Burkholder, J.B., Friedl, R.R., Golden, D.M., Huie, R.E., et al., 2011. Chemical Kinetics and Photochemical Data for Use in Atmospheric Studies, Evaluation Number 17. Hg. v. JPL Publication 10-6, Jet Propulsion Laboratory, Pasadena. Online verfügbar unter <http://jpldataeval.jpl.nasa.gov>.
- Schofield, Keith, 1978. Rate constants for the gaseous interaction of $O(2^1D_2)$ and $O(2^3S_0)$ – a critical evaluation. *J. Photochem.* 9 (1), 55–68. [https://doi.org/10.1016/0047-2670\(78\)87006-3](https://doi.org/10.1016/0047-2670(78)87006-3).
- Schunk, Robert W., Nagy, Andrew F., 2009. *Ionospheres. Physics, Plasma Physics, and Chemistry*. 2. Aufl. Cambridge Univ. Press, Cambridge and others.
- Scott, Graham B., Fairley, David A., Freeman, Colin G., McEwan, Murray J., Spanel, Patrik, Smith, David, 1997. Gas phase reactions of some positive ions with atomic and molecular hydrogen at 300 K. *J. Chem. Phys.* 106 (10), 3982–3987. <https://doi.org/10.1063/1.473116>.
- Scott, Graham B.I., Fairley, David A., Freeman, Colin G., McEwan, Murray J., Anicich, Vincent G., 1998. Gas-phase reactions of some positive ions with atomic and molecular nitrogen. *J. Chem. Phys.* 109 (20), S. 9010–9014. <https://doi.org/10.1063/1.477571>.
- Scott, Graham B.I., Fairley, David A., Milligan, Daniel B., Freeman, Colin G., McEwan, Murray J., 1999. Gas phase reactions of some positive ions with atomic and molecular oxygen and nitric oxide at 300 K. *J. Phys. Chem. A* 103 (37), 7470–7473. <https://doi.org/10.1021/jp9913719>.
- Seiff, Alvin, Kirk, Donn B., 1977. Structure of the atmosphere of Mars in summer at mid-latitudes. *J. Geophys. Res.* 82 (28), 4364–4378.
- Shinagawa, H., Miyoshi, Y., Jin, H., Fujiwara, H., 2017. Global distribution of neutral wind shear associated with sporadic E layers derived from GAIA. *J. Geophys. Res. Space Physics* 122 (4), 4450–4465.
- Shuman, Nicholas S., Hunton, Donald E., Viggiano, Albert A., 2015. Ambient and modified atmospheric ion chemistry: from top to bottom. *Chem. Rev.* 115 (10), 4542–4570. <https://doi.org/10.1021/cr5003479>.
- Soffen, Gerald A., 1977. The viking project. *J. Geophys. Res.* 82 (28), 3959–3970.
- Stancil, P.C., Schultz, D.R., Kimura, M., Gu, J.-P., Hirsch, G., Buenker, R.J., 1999. Charge transfer in collisions of O^+ with H and H^+ with O. *Astron. Astrophys. Suppl. Ser.* 140 (2), S. 225–234. <https://doi.org/10.1051/aas:1999419>.
- Stevens, Michael H., Siskind, David E., Evans, J. Scott, Fox, Jane L., Deighan, Justin, Jain, Sonal K., Schneider, Nicholas M., 2019. Detection of the nitric oxide dayglow on Mars by MAVEN/IUVS. *J. Geophys. Res.* 11 (7) <https://doi.org/10.1029/2019JE005945>. S. 3158.
- Stiepen, A., Jain, S.K., Schneider, Nicholas M., Deighan, J.I., González-Galindo, Francisco, Gérard, J.-C., et al., 2017. Nitric oxide nightglow and Martian mesospheric circulation from MAVEN/IUVS observations and LMD-MGCM predictions. *J. Geophys. Res.* 122 (5), S. 5782–5797. <https://doi.org/10.1002/2016JA023523>.
- Terada, Naoki, Leblanc, F., Nakagawa, Hiromu, Medvedev, Alexander S., Yiğit, Erdal, Kuroda, Takeshi, et al., 2017. Global distribution and parameter dependences of gravity wave activity in the Martian upper thermosphere derived from MAVEN/NGIMS observations. *J. Geophys. Res. Space Physics* 122 (2), 2374–2397.
- Tobiska, W. Kent, Woods, Tom, Eparvier, Frank, Viereck, Rodney, Floyd, Linton, Bouwer, Dave, et al., 2000. The SOLAR2000 empirical solar irradiance model and forecast tool. *J. Atmos. Sol. Terr. Phys.* 62 (14), S. 1233–1250. [https://doi.org/10.1016/S1364-6826\(00\)00070-5](https://doi.org/10.1016/S1364-6826(00)00070-5).
- Tsang, W., Hampson, R.F., 1986. Chemical kinetic data base for combustion chemistry. Part I. Methane and related compounds. *J. Phys. Chem. Ref. Data* 15 (3), 1087–1279. <https://doi.org/10.1063/1.555759>.
- Ulusen, Demet, Brain, David A., Luhmann, Janet G., Mitchell, David L., 2012. Investigation of Mars’ ionospheric response to solar energetic particle events. *J. Geophys. Res.* 117 (A12) <https://doi.org/10.1029/2012JA017671>.
- Viggiano, A.A., Knighton, W.B., Williams, Skip, Arnold, Susan T., Midey, Anthony J., Dotan, I., 2003. A reexamination of the temperature dependence of the reaction of N^+ with O_2 . *Int. J. Mass Spectrom.* 223–224, 397–402. [https://doi.org/10.1016/S1387-3806\(02\)00925-9](https://doi.org/10.1016/S1387-3806(02)00925-9).
- Viggiano, A.A., Ehlerding, A., Hellberg, Fredrik, Thomas, R.D., Zhaunerchik, V., Geppert, Wolf D., et al., 2005. Rate constants and branching ratios for the dissociative recombination of CO_2^+ . *J. Chem. Phys.* 122 (22) <https://doi.org/10.1063/1.1926283>. S. 226101.
- von Zahn, U., Fricke, K.H., Hunton, Donald E., Krankowsky, D., Mauersberger, K., Nier, A.O., 1980. The upper atmosphere of Venus during morning conditions. *J. Geophys. Res.* 85 (A13) <https://doi.org/10.1029/JA085iA13p07829>. S. 7829.
- Wang and Nielsen, 2003. Behavior of the Martian dayside electron density peak during global dust storms. *Planet. Space Sci.* 51 (4–5), 329–338.
- Wedunby, C.S., Gronoff, G., Liliensten, J., et al., 2011. Comprehensive calculation of the energy per ion pair or W values for five major planetary upper atmospheres. *Ann. Geophys.* 29 (1), 187–195.
- Whalley, Charlotte L., Plane, John M.C., 2010. Meteoric ion layers in the Martian atmosphere. *Faraday Discuss.* 147, 349–368. <https://doi.org/10.1039/c003726e>.
- Whitehead, J.D., 1960. Formation of the sporadic E layer in the temperate zones. *Nature* 188, S. 567.
- Withers, Paul, 2009. A review of observed variability in the dayside ionosphere of Mars. *Adv. Space Res.* 44 (3), 277–307. <https://doi.org/10.1016/j.asr.2009.04.027>.
- Withers, Paul, Mendillo, Michael, Hinson, David P., Cahoy, K., 2008. Physical characteristics and occurrence rates of meteoric plasma layers detected in the Martian ionosphere by the Mars Global Surveyor Radio Science Experiment. *J. Geophys. Res.* 113 (A12) <https://doi.org/10.1029/2008JA013636>.
- Withers, Paul, Felici, M., Mendillo, M., Moore, L., Narvaez, C., Vogt, M.F., Jakosky, B.M., 2018. First Ionospheric results from the MAVEN radio occultation science experiment (ROSE). *J. Geophys. Res.* 123 (5), 4171–4180. <https://doi.org/10.1029/2018JA025182>.
- Woods, Thomas N., Tobiska, W. Kent, Rottman, Gary J., Worden, John R., 2000. Improved solar Lyman α irradiance modeling from 1947 through 1999 based on UARS observations. *J. Geophys. Res.* 105 (A12), 27195–27215. <https://doi.org/10.1029/2000JA000051>.
- Yiğit, Erdal, Medvedev, Alexander S., 2015. Internal wave coupling processes in Earth’s atmosphere. *Adv. Space Res.* 55 (4), 983–1003.
- Yiğit, Erdal, England, Scott L., Liu, Guiping, Medvedev, Alexander S., Mahaffy, Paul R., Kuroda, Takeshi, Jakosky, Bruce M., 2015. High-altitude gravity waves in the Martian thermosphere observed by MAVEN/NGIMS and modeled by a gravity wave scheme. *Geophys. Res. Lett.* 42 (21), S. 8993–9000.
- Yiğit, Erdal, Knížová, Koucká, Petra, Georgieva, Katya, Ward, William, 2016. A review of vertical coupling in the Atmosphere–Ionosphere system: effects of waves, sudden stratospheric warmings, space weather, and of solar activity. *J. Atmos. Sol. Terr. Phys.* 141, 1–12.